1

2

3   **Control of Epithelial Tissue Organization by mRNA Localization**

4

5

6   Devon E. Mason[1]*, Thomas D. Madsen[1], Alexander N. Gasparski[1], Neal Jiwnani[1], Terry

7   Lechler[2,3], Roberto Weigert[1], Ramiro Iglesias-Bartolome[1], Stavroula Mili[1]*

8

9

10

11   [1] Laboratory of Cellular and Molecular Biology, Center for Cancer Research, National Cancer

12   Institute, NIH, Bethesda, MD, USA

13   [2] Department of Dermatology, Duke University Medical Center, Durham, NC, USA

14   [3] Department of Cell Biology, Duke University Medical Center, Durham, NC, USA

15

16

17   * Correspondence: voula.mili@nih.gov

18   devon.mason@nih.gov

19

20

21

22

23

24

25   Laboratory of Cellular and Molecular Biology

26   NCI, NIH

27   37 Convent Drive, MSC 4256

28   Building 37, Room 2042

29   Bethesda, MD 20892-4256

30   Tel: 240-760-6844

31

32 **Abstract**

33

34   mRNA localization to specific subcellular regions is common in mammalian cells but

35   poorly understood in terms of its physiological roles[1-6,7]. This study demonstrates the functional

36   importance of *Net1* mRNA, which we find prominently localized at the dermal-epidermal junction

37   (DEJ) in stratified squamous epithelia. *Net1* mRNA accumulates at DEJ protrusion-like structures

38   that interact with the basement membrane and connect to a mechanosensitive network of

39   microfibrils. Disrupting *Net1* mRNA localization in mouse epithelium alters DEJ morphology and

40   keratinocyte-matrix connections, affecting tissue homeostasis. mRNA localization dictates Net1

41   protein distribution and its function as a RhoA GTPase exchange factor (GEF). Altered RhoA

42   activity is in turn sufficient to alter the ultrastructure of the DEJ. This study provides a high-

43   resolution *in vivo* view of mRNA targeting in a physiological context. It further demonstrates how

44   the subcellular localization of a single mRNA can significantly influence mammalian epithelial

45   tissue organization, thus revealing an unappreciated level of post-transcriptional regulation that

46   controls tissue physiology.

47

48

Main

mRNA localization has emerged as a prevalent level of post-transcriptional regulation not only in model systems but also in higher organisms. Indeed, in diverse mammalian cell types, a large fraction of the transcriptome is targeted to specific subcellular destinations and adopts distinct distribution patterns[1-7]. Nevertheless, whether the localization of individual mRNAs is important for mammalian physiology remains poorly characterized, especially in tissues outside the nervous system[8,9].

A well-studied localization pathway targets mRNAs to peripheral protrusions of mammalian mesenchymal cells through active kinesin-dependent trafficking on microtubules[7,10-12]. Localization to protrusions of mRNAs, such as *NET1* and *RAB13*, plays an important role in mesenchymal migration in cultured cell systems[13-16]. Mechanistically, mRNA location specifies the site of protein synthesis, which can influence the function of the encoded polypeptide. Specifically, mRNA targeting to particular local micro-environments promotes certain co-translational interactions of the nascent protein thus guiding binding partner selection[13,15,17]. In the case of NET1, localization of *NET1* mRNA at protrusions promotes NET1 protein association with a membrane-bound scaffold[15]. Plasma membrane-associated NET1 acts as a guanine nucleotide exchange factor (GEF) for the small GTPase RhoA, a central regulator of the cytoskeleton[18,19]. In contrast, perinuclear *NET1* mRNA promotes nascent NET1 binding to importins leading to its nuclear sequestration. In this way, the location of the *NET1* mRNA modulates cytoskeletal dynamics and influences complex cellular processes like mesenchymal cell migration *in vitro*[15]. Protrusion-localized mRNAs, including *NET1*, have also been observed at the basal surface of *in vitro* cultured epithelial cells as well as in intestinal enterocytes *in vivo*[1,2]. However, the functional significance of this epithelial basal localization is unknown.

Here we examine the functional role of protrusion mRNA localization in mouse epithelial physiology. We find that, strikingly, protrusion-localized mRNAs are targeted to uncharacterized protrusion-like structures formed by basal keratinocytes in mammalian stratified epithelial tissue. These formations at the dermal-epidermal junction (DEJ) are connected to mechanosensitive microfibrils in the extracellular matrix. Using specific, sequence-blocking anti-sense oligos to prevent *Net1* mRNA localization to the DEJ, we show that *Net1* mRNA location is necessary for maintaining DEJ architecture and epithelial homeostasis through the RhoA pathway. This study connects mRNA localization to unexplored aspects of epithelial physiology and highlights this

80 prevalent level of post-transcriptional regulation as an important contributor to tissue function in

81 higher organisms.

82

83 **Results**

84 *Basal accumulation of Net1 mRNA is conserved across epithelial tissues*

85

86   To probe the function of protrusion-localized mRNAs in epithelia *in vivo*, we first surveyed

87 the localization of several protrusion localized mRNAs[11,20] (i.e. *Net1, Cyb5r3, Palld, Kif1c, Pkp4*)

88 across various mouse epithelial tissues that are architecturally distinct. These tissues included

89 monolayered tubular epithelial structures (intestine and kidney) as well as stratified squamous

90 epithelia (tongue and skin) (Fig. 1a). To allow spatial quantitative assessments, RNA detection was

91 accompanied by staining with a combination of wheat germ agglutin (WGA) and β-catenin to

92 delineate overall tissue architecture and cell borders (Fig. 1b and Extended Data Fig. 1a,b). To

93 permit comparison across tissues, we focused in each case on the basal layer of cells in contact

94 with the extracellular basement membrane (BM). The BM was demarcated by WGA providing a

95 comparable basal boundary between BM-associated cells in different tissues. Tissues were

96 manually segmented as individual layers (Fig. 1a,b and Extended Data Fig. 1a,b; BM marked by

97 a yellow dashed line) and RNA signal was quantified along the apico-basal axis (Fig. 1c). We

98 define the RNA amount in the 30% basal part of this epithelial layer as the 'basal mRNA fraction'

99 (Fig. 1c and Extended Data Fig. 1a). Interestingly, most of the tested mRNAs accumulate in the

100 basal part of the epithelial layer, as opposed to the non-targeted control *Gapdh* mRNA (Fig. 1d and

101 Extended Data Fig. 1c). There was also evident variability in basal mRNA targeting both among

102 tissues and between protrusion-localized mRNAs, suggesting transcript- and tissue-specific

103 differences in the magnitude of mRNA localization. Nevertheless, mRNAs like *Net1* and *Cyb5r3*

104 emerged as consistently basally localized mRNAs in all tissues tested.

105   To look further into these candidates, we surveyed published RNA-seq and tissue RNA

106 imaging datasets. Interestingly, *Net1* is specifically enriched in basal cells of the skin and tongue;

107 *Net1* is also nearly 4-times as abundant as the 5 next most highly expressed Rho-family GEFs

108 (Extended Data Fig. 1d, e)[21-23]. Furthermore, *Net1* expression is 9-times higher in keratinocytes

109 than dermal fibroblasts of the skin pointing to a potential important function in the epidermal

110 compartment (Extended Data Fig. 1d)[21]. In addition, we characterized the *in vivo NET1* mRNA

111 distribution in stratified epithelial tissues of other species by examining primate tongue and human

112 skin biopsies. Importantly, we again found in these cases that *NET1* mRNA exhibits a significant

113 basal enrichment suggesting that basal *NET1* mRNA localization is evolutionarily conserved (Fig.

114 1a,d). We thus focused on the mouse *Net1* mRNA for further molecular and functional

115 characterization utilizing the stratified tongue epithelium as an amenable experimental system.

116   The stratified squamous epithelium of the tongue consists of epithelial cells at different

117 proliferation and differentiation states. Basal keratinocytes attached to the BM can enter the cell

118 cycle and upregulate proliferating cell nuclear antigen (PCNA) during S/G2/M-phases[24]. To see

119 whether *Net1* mRNA localization differs between quiescent and proliferating basal cells, we

120 measured basal *Net1* accumulation in PCNA^{Hi} and PCNA^{Lo} cells (Fig. 1e). *Net1* distribution was

121 not significantly different between cell proliferation states, based on this cell division marker (Fig.

122 1f). Basal Krt5+ cells can additionally transition to the suprabasal layer while upregulating

123 differentiation markers like keratin 13 (Krt13) in the mouse tongue. As a result, such Krt13+ cells

124 eventually lose contact with the BM. Quantification of *Net1* mRNA amount (by RNA-FISH)

125 showed that *Net1* is downregulated in suprabasal differentiated keratinocytes (Extended Data Fig.

126 1e). Interestingly, we could detect cells that appear to be in the process of delaminating, since they

127 exhibit basally-oriented Krt13 cellular extensions intercalating between Krt5+ cells (Fig. 1g). Such

128 cells exhibited accumulation of *Net1* mRNA at the tips of these extensions, albeit infrequently

129 (Fig. 1g inset). We interpret this to suggest that basal *Net1* mRNA localization is transiently

130 maintained in delaminating keratinocytes concomitantly with an overall *Net1* downregulation

131 during differentiation. Overall, these data suggest that *Net1* mRNA expression and localization is

132 notably elevated in BM-contacting keratinocytes, regardless of their proliferation state. We

133 therefore focused our attention on characterizing *Net1* mRNA and its function in basal

134 keratinocytes.

135

136 *Net1 mRNA accumulates in protrusion-like structures that contact microfibrils at the dermal*

137 *epidermal junction*

138

139   Basal cells of the tongue reside at the interface between the oral epithelium and the

140 underlying connective tissue. This interface in stratified epithelia has been primarily studied in the

141 skin and referred to as the dermal-epidermal junction (DEJ). We will be using the same

142   terminology here, given the parallels between oral and skin tissue[25]. The DEJ includes the basal

143   plasma membrane and specialized adhesions called hemidesmosomes, which connect the

144   epithelium to the BM and the dermal extracellular matrix (ECM) through fibrillar anchoring

145   complexes[26,27]. The DEJ has important roles in maintaining the epithelium both by acting as a

146   reservoir for signaling molecules and by providing structural support[28,29].

147   We performed high-resolution confocal imaging of the DEJ, because of the pronounced

148   basal accumulation of the *Net1* mRNA. We specifically visualized the basal cell membrane through

149   staining with integrin a6 (Itga6), a core hemidesmosome component. Strikingly, high-resolution

150   imaging revealed a high degree of topographical variability of the basal membrane which consisted

151   of numerous micron- or submicron-wide protrusion-like structures that interdigitated with the BM

152   (Fig. 2a; full serial optical slices of these structures can be viewed in Supplementary Videos 1 and

153   2). While these topographically variable regions have been observed incidentally in older

154   literature[30,31], the associated components or potential function of these structures is unknown[32].

155   Notably, the *Net1* mRNA localized within, and quite frequently at the tips of these structures (Fig.

156   2a; yellow arrowheads). Despite their smaller size, these keratinocyte structures appear

157   morphologically similar to the *in vitro* cultured mesenchymal cell protrusions, where *Net1* and

158   other protrusion-localized mRNAs have been previously studied[13-15]. These data thus raise the

159   intriguing possibility that these uncharacterized keratinocyte structures reflect *in vivo* equivalents

160   of *in vitro* protrusion-like structures and are analogously associated with localized mRNAs,

161   including *Net1*.

162   Protrusion-like basal membrane structures can also be visualized upon staining with WGA

163   (Fig. 2b; serial optical slices can be viewed in Supplementary Videos 1 and 2). Aside from

164   visualizing the interdigitations this staining also revealed a complex fiber network that spans the

165   dermis and appears to connect with the protrusion-like structures at the DEJ (Fig. 2b; note that this

166   image presents a projection of multiple optical slices to allow better visualization of the fiber

167   network). To determine what these WGA+ fibers correspond to, we surveyed various components

168   of the DEJ and the dermal ECM. Co-detection with WGA indicated that these fibers are not

169   enriched for hemidesmosome (Col17a1), basement membrane (laminin), or anchoring fibril (Col7)

170   DEJ components (Extended Data Fig. 2). Because these fibers form an extensive network below

171   the DEJ, we hypothesized that they are part of the dermal ECM. However, detection of collagen I

172   (Col1a1), the primary dermal ECM component, showed that these fibers are not enriched for

173   Col1a1 except at regions proximal to the DEJ (Extended Data Fig. 2). We discovered, though, that

174   these fibers are strongly positive for fibrillin 2 (Fbn2), a major component of the microfibrils that

175   are part of the elastic fiber network which allows transmission of mechanical forces across the

176   dermis (Fig. 2c)[33-37]. Given the fact that stratified squamous epithelium is regularly mechanically

177   deformed and that the microfibrils are essential in resisting this deformation, it is tempting to

178   speculate that keratinocyte protrusions are sites of high mechanical stress. Pertinent to this,

179   targeting of protrusion-localized mRNAs in *in vitro* cultures is coordinated with cellular

180   mechanical state and influenced by ECM properties in various settings[11,16]. Therefore, the DEJ

181   could reflect a physiological setting where the mechanoresponsive localization of mRNAs is

182   particularly relevant.

183

184   *Net1 mRNA localization is necessary for maintaining epithelial architecture and protrusion-like*

185   *structures at the DEJ*

186

187   To broadly address the functional role of *Net1* mRNA localization in epithelial physiology,

188   and protrusion-like structures specifically, we employed sequence blocking phosphorodiamidate

189   morpholino oligos (PMOs). PMOs antisense to GA-rich regions of human protrusion-localized

190   mRNAs have been shown to specifically prevent the localization of the targeted mRNA by

191   blocking the formation of a transport-competent complex between the mRNA and the KIF1C

192   kinesin[14,15,38]. To determine whether we can extend the use of this approach to mice, we designed

193   PMOs that target the analogous GA-rich regions in the mouse *Net1* 3'UTR and tested them in *in*

194   *vitro* cultured mouse NIH/3T3 fibroblasts. PMOs were either targeted to *Net1* GA-rich regions

195   (PMOs #992 and #1016) or another downstream area (PMO #1620), or to an unrelated sequence

196   (control PMO) (Extended Data Fig. 3a). Indeed, GA-targeting PMOs, but not other sequences,

197   significantly prevented the localization of the *Net1* mRNA to the periphery of 3T3s without

198   affecting another protrusion localized mRNA, *Cyb5r3* (Extended Data Fig. 3b, c). Importantly,

199   and consistent with prior reports in human cells, the effect on *Net1* mRNA localization was not

200   accompanied by any detectable change in the amount of *Net1* mRNA (Extended Data Fig. 3d)[15].

201   We also measured the enrichment of various mRNAs within isolated 3T3 protrusions and observed

202   that Net1 PMO delivery affected solely the enrichment of the *Net1* mRNA while all other detected

203   transcripts were unaffected (Extended Data Fig. 3e). We further validated that Net1 PMOs #992

204   and #1016 can similarly disrupt *Net1* mRNA localization in an immortalized keratinocyte cell line

205   *in vitro* (Extended Data Fig. 4a,b), again without affecting *Net1* mRNA levels or the amount of

206   Net1 protein produced (Extended Data Fig. 4c-e). These data confirm the broad conservation of

207   the mRNA trafficking mechanisms to protrusions, and the applicability of PMO delivery as a

208   specific tool to modify mRNA distributions in diverse cell types.

209   To assess the physiological importance of *Net1* mRNA localization *in vivo* we

210   intradermally injected the two *Net1* localization altering PMOs or two control PMOs (one targeting

211   GFP and one corresponding to a scrambled Net1 #992 sequence) into mouse tongues. PMOs were

212   administered every 2 days over 6 days (Fig. 3a). We confirmed, by small RNA in situ hybridization,

213   that PMOs reached and were taken up by the cells in the epithelium (Fig. 3b). Significantly, when

214   we measured *Net1* mRNA distribution in injected tissues, there was a substantial reduction in the

215   fraction of basal *Net1* mRNA upon administration of the GA-rich region targeting PMOs (Fig.

216   3c,d). Therefore, PMOs can prevent the basal accumulation of the endogenous *Net1* mRNA in

217   epithelial tissues *in vivo*.

218   Further phenotypic analysis revealed prominent defects in epithelial architecture detected

219   by H&E staining (Fig. 3e). Specifically, the epithelium of Net1 PMO-treated tongue epithelia was

220   thinner in comparison to control treated tissues (Fig. 3f). Such changes in epithelial architecture

221   can be brought about by defects in cellular differentiation[39,40]. Visualization of canonical markers

222   of the basal and spinous compartment, Krt5 and Krt13 respectively, revealed that Net1 PMO-

223   treated tongue contained significantly more Krt5/Krt13+ double positive cells in the basal layer

224   (Fig. 3g-i). This suggests either spontaneous differentiation of Krt5+ cells or alternatively a defect

225   in cell detachment from the basement membrane.

226   Given the fact that *Net1* mRNA localizes to protrusion-like structures at the DEJ, we

227   investigated whether altering *Net1* localization from the basal surface affects DEJ organization.

228   Indeed, Net1 PMO-treated epithelium exhibited drastic flattening of protrusion-like structures

229   formed by basal keratinocytes (Fig. 3j). We quantified this change by measuring topographical

230   variation of the DEJ using optical slices of the Itga6-stained basal membrane (Extended Data Fig.

231   5). Using this metric, DEJ variation was halved in Net1 PMO-treated epithelia (Fig. 3k). As shown

232   above, basal protrusions appear to be connected to Fbn2+ fibers. We thus asked whether altering

233   *Net1* localization has broader effects on the microfibrils near the DEJ. Consistent with this, the

234   volume of Fbn2+ fibers was significantly reduced in regions proximal to the DEJ (Fig. 3l,m). This

235   result could reflect ECM remodeling near the epithelium but may also be due to decreased

236   antibody-epitope accessibility on individual fibers due to altered mechanical strain, which can lead

237   to changes in fibrillin domain folding[41]. Regardless, it is notable that dysregulation of the DEJ

238   during aging or in genetic diseases, including ones caused by mutations in fibrillins, has strong

239   negative implications on epidermal physiology[32,33,37,42]. Altogether, these results demonstrate that

240   altering the basal localization of a single mRNA, *Net1,* is sufficient to drastically influence

241   keratinocyte physiology and tissue homeostasis, potentially by altering interactions of the basal

242   epithelium with the DEJ.

243

244   *Net1 mRNA localization controls Net1 protein distribution and activity in vivo*

245

246   To understand the mechanism through which altering *Net1* mRNA localization affects

247   keratinocyte physiology, we considered that *Net1* mRNA location might affect the activity of the

248   encoded Net1 protein as a RhoA GEF. Net1 is quite unique among RhoA regulators in that it is

249   controlled by nucleo-cytoplasmic trafficking[43,44]. While RhoA activation largely occurs at the

250   plasma membrane, Net1 can be imported and sequestered in the nucleus, providing an "off-switch"

251   for Net1-dependent RhoA activation[15,18]. *Net1* mRNA location balances Net1 nuclear import

252   versus cytoplasmic retention by a partner-selection mechanism in mesenchymal cells *in vitro*.

253   Specifically, translation of Net1 from protrusion-localized mRNA favors its interaction with a

254   membrane scaffold and promotes RhoA activation by Net1[15]. To determine whether this mRNA

255   location-dependent regulation operates in the tongue epithelium *in vivo,* we looked at the

256   subcellular distribution of the Net1 protein. We first validated the specificity of the Net1 antibody,

257   by immunofluorescence staining of immortalized keratinocytes upon Net1 knock down with two

258   different siRNAs (Extended Data Fig. 6a,b). We then observed Net1 protein distribution in tongue

259   sections. Net1 protein signal was primarily detected in the basal epithelial layer (Fig. 4a),

260   consistent with the basal cell specific expression pattern of *Net1* mRNA, mentioned above

261   (Extended Data Fig. 1e). This further supports the specificity of Net1 protein detection. We note

262   that while Net1 protein is primarily nuclear in cultured keratinocytes, in *in vivo* tissue Net1 is

263   primarily cortical (compare Fig. 4a and Extended Data Fig. 6a). While the basis for this differential

264   regulation is still unclear, this has been also observed in other studies[18,45,46]. Additionally, Net1 is

265   observed throughout the basal keratinocyte cortex (Fig. 4a), consistent with *in vitro* results

266 showing that Net1 retained in the cytoplasm can distribute away from the site of protein

267 synthesis[15]. To quantify changes in Net1 protein distribution we measured its cortical/non-cortical

268 intensity (Fig. 4a-c). Net1 PMO-treated epithelium showed a reduced cortical Net1 accumulation

269 (Fig. 4d), indicating that *Net1* mRNA location controls Net1 protein distribution *in vivo.*

270 A reduction in cortical Net1 amount would be predicted to result in reduced activation of

271 the RhoA GTPase. Given that it is technically difficult to directly measure RhoA activity in tissues,

272 we examined the phosphorylation of myosin light chain (pMLC), a major downstream RhoA

273 target[47]. pMLC levels were visualized using a phospho-specific antibody under conditions that

274 allow specific detection (Extended Data Fig. 7). Quantification of pMLC levels in Net1 PMO-

275 injected tongue epithelium revealed that altering *Net1* mRNA localization reduced pMLC in both

276 basal keratinocytes and more broadly across the entire epithelium (Fig. 4e,f). Therefore, preventing

277 the basal localization of the *Net1* mRNA leads to altered Net1 protein distribution and a reduction

278 in RhoA-pMLC signaling. Given that this pathway is well known to control cytoskeletal tension

279 and cell attachment, it is likely that it reflects the mechanism linking *Net1* mRNA targeting to DEJ

280 structure and epithelial organization.

281

282 *DEJ morphology is sensitive to fluctuations in basal keratinocyte cytoskeletal state*

283

284 To test this idea, we tried to independently address whether changes in RhoA signaling

285 within basal keratinocytes control their interaction with the DEJ. For this, we used a genetic system

286 for cell-type specific RhoA activation[48,49]. Krt14-rtTA mice were crossed with a genetic knock-in

287 of a constitutively active RhoA GEF, ArhGEF11 (ArhGEF11[CA]), under the control of a

288 tetracycline-inducible promoter (Fig. 5a), to achieve RhoA activation specifically in basal

289 keratinocytes. Doxycycline injection led to basal keratinocyte-specific overexpression of

290 ArhGEF11[CA] in mouse tongue, visualized by an HA-tag, as early as 10hrs post-injection (Fig. 5b).

291 ArhGEF11[CA]-expressing cells exhibited increased cortical pMLC and filamentous actin

292 (phalloidin staining) indicative of RhoA-induced cytoskeletal tension (Fig. 5b).

293 We examined tongue tissue architecture in these mice, comparing them to mice with the

294 ArhGEF11[CA] cassette that were not crossed with Krt14-rtTA mice (WT/ArhGEF11[CA]). We focused

295 our quantitative analysis on DEJ regions where all of the basal keratinocytes express the HA-

296 tagged ArhGEF11[CA]. Remarkably, this short-term induction of RhoA signaling was sufficient to

297 significantly increase the topographical variation of the basal plasma membrane at the DEJ (Fig.

298 5c,d). Concomitantly, DEJ proximal Fbn2+ fibers became more prominent and displayed a higher

299 overall volume in regions proximal to the epithelium (Fig. 5e,f). Given the short induction time

300 we favor the idea that increased fibrillin detection reflects, at least partly, increased epitope

301 accessibility through tension-induced unfolding, rather than solely an increase in their absolute

302 amount.

303   A unique feature observed upon ArhGEF11^{CA} expression was the occasional appearance of

304 Itga6 strands co-localizing with Fbn2+ fibers far below the overall level of the basal plasma

305 membrane (Fig. 5g). The fact that these do not appear under normal conditions suggests that they

306 are formed upon the supraphysiologic tension induced under our experimental setting. We envision

307 that fibrillin resistance to keratinocytes' tensile forces eventually leads to fiber retraction away

308 from the epithelium. In this scenario the residual tension in fibrillin fibers pulls portions of the

309 plasma membrane below the ordinary DEJ (Fig. 5g). The tight colocalization of Itga6 with fibrillin

310 suggests the existence of stable mechanical coupling between the keratinocyte plasma membrane

311 and microfibrils. These data provide orthogonal evidence that changes in RhoA activity, and

312 cytoskeletal tension, is sufficient to alter keratinocyte connections with the DEJ. Therefore, the

313 RhoA pathway is the likely mediator of the ultrastructural changes at the DEJ in response to

314 altering *Net1* mRNA localization. Overall, the evidence presented here reveals mRNA localization

315 as an unappreciated level of post-transcriptional regulation that controls the mechanical coupling

316 of the epithelium with the underlying connective tissue, which broadly affects tissue physiology.

317

318 **Discussion**

319

320   Post-transcriptional mRNA regulation has well known roles both in normal physiology as

321 well as in disease, exemplified for instance by miRNA-mediated regulation during development[50],

322 or the therapeutic modulation of splicing patterns[51]. Targeting of mRNAs to specific subcellular

323 domains has emerged as another widespread level of post-transcriptional mRNA control with the

324 potential to spatially alter the proteome at a subcellular level[3,4] and control protein function[15].

325 Nevertheless, the contribution of mRNA localization to mammalian physiology has remained

326 largely unexplored. Here, we demonstrate that the subcellular localization of an individual mRNA,

327 *Net1*, is an important regulator of epithelial tissue homeostasis. This observation underscores the

328   importance of this post-transcriptional regulatory mechanism in epithelial tissue physiology where

329   ~15-30% of the transcriptome is differentially polarized[1,2] and sensitive to physiological stimuli[1].

330   Notably, we show that the basally localized *Net1* mRNA is associated with protrusion-like

331   structures of keratinocytes that contact a mechanosensitive network of dermal microfibrils. We

332   speculate that these underappreciated structures at the DEJ may be mechanical connections

333   necessary for long range force transmission between the epidermis and dermis. Targeting of the

334   *Net1* mRNA at these DEJ structures is necessary for their formation and its loss results in

335   remodeling of the dermal ECM. Our evidence further suggests that these effects are mediated

336   through basal cell autonomous activation of RhoA. Indeed, Net1-mediated activation of RhoA is

337   necessary for collagen I remodeling in breast tissue[52] as well as basement membrane breakdown

338   during embryonic development[45]. The findings presented here indicate that such RhoA-regulated

339   cell-ECM interactions are mediated at least partly by localized translation of the *Net1* mRNA.

340   Interestingly, *Net1* mRNA localization is itself mechanosensitive, being affected by the properties

341   of the ECM[11,16], implying the existence of feedback regulation that maintains an RNA-dependent

342   mechanical homeostasis of the DEJ. This maintenance of homeostasis extends to keratinocyte

343   function, including differentiation, which is regulated by cell-autonomous and tissue-wide

344   variation in mechanical state[39,40].

345   Alterations in DEJ components, including breakdown of the microfibrillar network and a

346   morphological attenuation of keratinocyte protrusions, occurs during aging[32,42]. Genetic

347   conditions, termed fibrillinopathies, also affect fibrillins and have deleterious effects on epidermal

348   homeostasis[29,37,53]. We speculate that changes in basal localization of *Net1*, and likely other

349   protrusion mRNAs, might be a contributing component in the mechanical uncoupling of the

350   epidermis in aging and disease. Given that Net1 is widely expressed and consistently localized in

351   a variety of tissues it is possible that its unique regulatory mechanism is utilized for maintenance

352   of epithelium-ECM connections in additional tissues. Furter understanding of the dynamic control

353   and functional contributions of such events occurring at tissue interfaces will provide exciting new

354   directions and context for studying RNA transport and local regulation in mammalian physiology.

355

356

357

Author Contributions

D.E.M. and S.M. conceived the project and designed experiments. D.E.M. and T.D.M. performed experiments. D.E.M., A.N.G., N.J., T.L., R.W., R.I-B. and S.M. analyzed data. S.M. and D.E.M. wrote original manuscript. All authors reviewed and edited the manuscript.

Declaration of Interests

The authors declare no competing interests.

Data and Code availability

Previously published sequencing data that were reanalyzed here are available under accession codes (GSE129218 and GSE77197). All other data supporting the findings of this study and custom analysis codes are available from the corresponding authors on reasonable request.

386 **Methods**
387
388 **Animal handling and tissue collection**

389 All experiments involving animals were performed in accordance with guidelines set by
390 the Institutional Animal Care and Use Committees of the National Cancer Institute (National
391 Institutes of Health, Bethesda, MD) and Duke University (Durham, NC; Protocol #: A255-23-12).
392 All mice (4-12 weeks) were housed in sterile filter-capped cages, fed and watered ad libitum, in a
393 12:12 light-dark cycle animal facility.

394 For injections, custom octaguanidine dendrimer conjugated PMOs (Vivo-Morpholino,
395 GeneTools) that target *EGFP* or *Net1* mRNA were synthesized (Extended Data Table 1). PMOs (5
396 nmol/inj) and fluorescently labelled dextran (2.5 μg/inj.; Molecular probes; D1976) were mixed in
397 isotonic sterile saline. 10μL of the solution was subcutaneously injected in the ventral portion of
398 the tongues of anesthetized male and female C57BL/6/NCr mice (Charles River; age 10-12
399 weeks). Anesthesia was performed by brief exposure to 3% isoflurane followed by intraperitoneal
400 injection of 100mg/kg ketamine and 10 mg/kg xylazine. The tongues were injected with PMOs
401 every two days for a total of three injections. Mice were sacrificed for tissue collection 6 days after
402 the initial injection.

403 4-week-old TRE-Arhgef11/Krt14-rtTA mice (3 males and 3 females) were IP-injected with
404 25 mg/kg doxycycline (Sigma) 10 hours before sacrifice and tissue collection.

405 Tissue was collected from male and female euthanized mice (age 4-12 weeks) washed
406 gently in PBS then flash frozen in optimal cutting temperature compound (OCT; Fisher Healthcare;
407 4585). Tissue embedded OCT blocks were cut 8-10um thick on a Leica cryostat microtome
408 CM1860. Tissues were collected on positively charged slides (Rankin; 20290W) then stored at -
409 80C. The gross tissue morphology of each tissue was visualized by H&E staining (abcam;
410 ab245880).

411

412 **Mouse keratinocyte cell line generation**

413 Mouse keratinocytes were isolated from tail skin of mixed background mice (FVB/N and
414 C57) by physical separation of the epidermis and dermis from the hypodermis. Tail skin was
415 sterilized with 10% v/v betadine/iodine in PBS. Excised tissue was digested overnight at 4C using
416 2U/mL of dispase II (StemCell; 07913) diluted in .25% trypsin without EDTA (Gibco; 15050065).
417 After digestion the tissue was minced and mixed with media and antibiotics. Keratinocytes were

418   then isolated from the digest by sequential straining using 100 μm and 40 μm cell strainers. Cells

419   were cultured for one passage using EpiLife medium with 60 μM calcium (Gibco, Waltham, MA,

420   MEPI500CA), supplemented with Human Keratinocyte Growth Supplement (HKGS, Life

421   Technologies, S0015), mouse EGF (10 ng/ml, R&D Systems, Minneapolis, MN, 2028EG200), and

422   Y-27632 compound (10 μM, Tocris Bioscience, Bristol, United Kingdom, 12-541-0).

423   Keratinocytes were then immortalized by infecting with lentiviruses expressing SV40 Large T

424   Antigen (Addgene Plasmid #170255). Cells were selected with Hygromycin (200 ug/mL) for two

425   days and then cells were passed for two passages in EpiLife and described supplements. Then cells

426   were cultured in DMEM (Sigma-Aldrich Inc) containing 10% fetal bovine serum (FBS) (Sigma-

427   Aldrich Inc), antibiotic/antimycotic solution (Sigma-Aldrich Inc), mouse EGF (10 ng/ml, R&D

428   Systems, Minneapolis, MN, 2028EG200), and Y-27632 compound (10 μM, Tocris Bioscience,

429   Bristol, United Kingdom, 12-541-0), for at least two passages before experiments. Lentiviruses

430   were produced by transfecting Lenti-X 293T cells with pMD2.VSVG (Addgene plasmid #12259)

431   and psPAX2 (Addgene plasmid #12260). Lenti-X 293T cells were obtained from Takara Bio and

432   cultured in DMEM (Sigma-Aldrich) containing 10% fetal bovine serum (Sigma-Aldrich).

433

434   **Immunofluorescence and tissue staining**

435   Fresh frozen sections or cultured cells were fixed in 4% formaldehyde (Sigma; F8775) for

436   15-30 minutes at RT washed 3x2 minutes in PBS and permeabilized in 0.2% Triton-X-100 for 5-

437   20 minutes. Sections were washed in PBST and blocked for 1 hour in 3% bovine serum albumin

438   (BSA) and 2% goat serum (GS) in PBS. Antibodies were diluted in blocking buffer and incubated

439   overnight (Extended Data Table 2). Samples were washed 3x2minutes in PBST and incubated with

440   fluorophore conjugated secondary antibodies corresponding to the host species (Extended Data

441   Table 2; 1:500 in blocking buffer). Samples were washed with PBST 3x2 minutes then

442   counterstained with a fluorophore conjugated variation of wheat germ agglutin (Invitrogen;

443   W11261; 10ug/mL), phalloidin (Invitrogen; A12379), and/or DAPI. Tissue samples were mounted

444   using #1.5 coverglass (Fisher; 12544D) with either prolong glass or diamond mounting medium

445   (Invitrogen; P36980 or P36962) and allowed to set overnight at room temperature.

446   Phosphorylated-myosin light chain 2 (Thr18/Ser19) was detected in tissue samples using a

447   modified immunofluorescence protocol. Briefly samples were fixed in 4% formaldehyde for 3

448   hours at RT, washed 3x5 minutes in TBS then treated with 1% SDS diluted in TBS for 20 minutes

449   at RT with regular agitation. Samples were washed thoroughly in 3x5 minutes in TBST (0.1%

450   Tween-20). Samples were blocked in 3%BSA and 2% GS in TBS for 1 hour. pMLC specific rabbit

451   mAb (Cell signaling; 95777) was diluted in blocking buffer and incubated at 4C overnight.

452   Staining was completed as described above with TBS instead of PBS.

453   Specificity of the pMLC antibody was validated by pre-treating tissues with 4000U λ

454   phosphatase (NEB; P0753S) diluted in 1xNEBuffer for protein phosphatases and 1mM $MnCl_2$

455   overnight at 30°C. Samples were washed thoroughly in TBST before proceeding with the staining

456   protocol described above.

457

458   **Cell culture**

459   NIH/3T3 mouse fibroblast cells (ATCC) were grown in Dulbeco's Modified Eagle Medium

460   (DMEM; Gibco; 11995-065) supplemented with 10% calf serum (Cytiva; SH30087.04), sodium

461   pyruvate, and penicillin/streptomycin (Gibco; 15140122). Immortalized mouse keratinocytes were

462   cultured in DMEM supplemented with 10% Fetal Bovine Serum,10ng/mL mouse EGF, and 10 μM

463   Y27632. Cells were cultured at 37°C, 5% CO_2 and passaged with either 0.05% (3T3) or 0.25%

464   (keratinocytes) trypsin with EDTA (Gibco; 25300054 or 25200056). Cells used in this study have

465   tested negative for mycoplasma.

466   For PMO delivery, cells were grown to 70% confluence in 12 well plates then transfected

467   with the indicated PMOs at a concentration of 15 μM in basal media. For small interfering RNA

468   (siRNA) experiments cells were cultured to 50-70% confluency in 6 or 12 well plates then

469   transitioned to antibiotic free media. Cells where transfected with the indicated siRNA (Qiagen;

470   final concentration 40 nM; Extended Data Table 1) which were pre-complexed with Lipofectamine

471   RNAimax (Invitrogen; 13778075) transfection reagent according to the manufacturer's

472   instructions. Cells were assayed for protein expression 48 hours after transfection.

473

474   **Imaging**

475   Fixed samples were imaged on a Nikon Eclipse Ti2-E inverted microscope with a

476   Yokogawa CSU-X1 spinning disk confocal scanner unit and operated using NIS-Elements

477   software. Images were acquired using 20x (Plan Apo 20x; NA = 0.75; WD = 1000μm), 40x (Plan

478   Fluor 40; Oil; NA = 1.30; WD = 240 μm), 60x (Apo 60x λS DIC N2; Oil; NA = 1.40; WD = 140

479   μm), or 100x (Apo TIRF DIC N2; Oil; NA = 1.49; WD = 120 μm) objectives and a Hamamatsu

480   ORCA-Fusion BT Gen III back-illuminated sCMOS cameras. Images were denoised and

481   deconvolved using the Richardson-Lucy algorithm in the NIS-Elements analysis software.

482   Whole sample brightfield images of H&E-stained samples were taken using a Zeiss Axio

483   Scan.Z1 (Zeiss) equipped with a Hamamatsu OrcaFlash 4.0 camera using 10x and 20x objectives.

484   Images were aquired using the Carl Zeiss Zen 2.3 software and analyzed using the HALO image

485   analysis platform (Indica Labs).

486

487   **Basal mRNA quantification**

488   mRNA accumulation to the basal region of epithelial layers was quantified by manually

489   segmenting a maximum projection of ~1 μm thick optical sections in MATLAB (Mathworks;

490   R2021b-R2023b). A custom script was used to separate the segmented layer into 10 evenly divided

491   bins from the basal to apical side of a layer, and to measure fluorescent intensity in each bin after

492   a uniform background subtraction. The fraction of intensity in each bin was then calculated per

493   layer and used to measure relative fraction of basal mRNA (bottom 30% of a segmented layer).

494

495   **Net1 protein distribution**

496   Net1 protein distribution was calculated on a per cell basis by manually segmenting basal

497   keratinocytes in the mouse tongue using the FIJI image analysis platform[54]. Segmentation was

498   performed on individual optical slices taken with a 100x objective described above. Cortical Net1

499   protein mean intensity was measured in the peripheral 15% of the cell then normalized to the most

500   central 65% of the segmented cell.

501

502   **DEJ variation analysis**

503   To measure the complex protrusion-like structures at the DEJ we decided to use a metric

504   that incorporates DEJ topographical variation (the full process is visualized in Extended Data Fig.

505   5). Briefly, the DEJ was manually segmented into individual optical slices using the FIJI line tool

506   (120 pixel centered on the DEJ). Itga6 fluorescent intensity was automatically thresholded and

507   skeletonized. The basal cell membrane was estimated for each x-position using the skeletonized

508   image. The x- and y- coordinates from these measurements were then used to create a 2D plot

509   profile from which the absolute distance between the basal cell membrane and the segmentation

510   line was measured for each x-coordinate. Distances were summed and normalized to the number

of x-positions measured to yield a single DEJ variation metric. This analysis approach is analogous to the surface characterization strategies common in machining applications[55].

Fibrillin 2+ quantification analysis

Fibrillin 2+ fiber volume was measured using 4 μm thick optical stacks acquired from epidermis proximal dermal areas (~50 μm^2) using a 100x objective. Imaris (Bitplane; v9.9.0) was used to generate Fbn2+ fiber volumes by thresholding Fbn2 fluorescence intensity equally between samples within a given experiment. Morphological filters were then equally applied across conditions to remove small spherical volumes that were not consistent with fiber segments. The cumulative fiber volume was then measured from all extracellular Fbn2+ fiber volumes in each image.

Peripheral distribution index analysis

FISH images of *in vitro* cultured cells were analyzed using a previously published MATLAB script[56]. Briefly, the peripheral distribution index (PDI) of individual RNAs was measured by calculating the difference between the geometric centroid of a cell and the intensity weighted centroid of an RNA. This value is then normalized to a hypothetical uniformly distributed RNA. This ratio represents the relative peripheral distribution of an RNA in the context of a cell's geometry. RNAs are considered peripheral if PDI values are greater than 1, homogenous if equal to 1, and perinuclear if less than 1.

RNA detection

Detection of RNA in tissues sections was performed using the RNAscope Multiplex Fluorescent Reagent kit v2 (ACD; 323100). Tissues were first pre-processed as follows: fresh frozen tissues were fixed for 45 minutes in 4% formaldehyde (Sigma) diluted in PBS at room temperature. Samples were washed 3x2 minutes in PBS then sequentially dehydrated in EtOH (50, 70, 100%) and rehydrated in hydrogen peroxide (ACD). Samples were washed twice in distilled water then PBST (0.1% Tween-20). If proteins were co-detected, then antibodies were diluted in Co-Detection Antibody Diluent (ACD; 323160). Antibodies were incubated overnight at 4C after the hydrogen peroxide step. Samples were washed 3x2 minutes in PBST. Then the antibodies were fixed for 30 minutes using 4% formaldehyde then washed 3x2 minutes in PBST. Protease IV

542 (ACD) was applied for 30 minutes at RT washed 3x in deionized water. Primary RNA probes

543 (Extended Data Table 3) were applied, and the detection protocol was completed according to

544 manufacturer's instructions. Tissues were then counterstained with AF488 conjugated wheat germ

545 agglutin, fluorescently labelled secondary antibodies, and DAPI.

546 PMOs were detected using the RNAscope Plus smRNA-RNA HD detection kit (ACD;

547 322780) according to the protocol described above and the manufacturer's instructions. PMO

548 detection probes were used at 1:1,000 of the manufacturer's recommended concentration.

549 For RNA detection in NIH/3T3 cells or mouse keratinocytes, cells were plated on Collagen

550 IV-coated (10 μg/mL; Sigma; C5533) #1.5 glass coverslips for 2-3 hours at 37C. Cells were fixed

551 for 20 minutes at RT in 4% paraformaldehyde (EMS; 15710) then processed using the ViewRNA

552 ISH Cell assay kit (Thermo Fisher Scientific; QVC0001) according to the manufacturer's

553 instructions and probes for individual mRNAs (Extended Data Table 3). Cell mask and DAPI were

554 used as counterstain to detect the cell periphery and nucleus. Samples were mounted in prolong

555 gold.

556

557 **RNA isolation and ddPCR**

558 Bulk RNA was isolated from *in vitro* cultured cells using either Trizol LS (Thermo Fisher

559 Scientific; 10296010) or RNeasy Plus Mini kit (Qiagen; 74134). 1μg of RNA was reverse

560 transcribed using the iScript cDNA Synthesis Kit (Bio-Rad; 1768891) and used for droplet digital

561 polymerase chain reaction (ddPCR). PCR reactions were prepared with cDNA, gene specific

562 primers, and ddPCR EvaGreen Supermix (Bio-Rad; 186-4034). Droplets were generated from this

563 reaction using the Automated Droplet Generator (Bio-Rad; 186-4101), PCR was then performed

564 on a C1000 Touch Thermal Cycler (Bio-Rad; 185-1197), and droplet reading was performed on

565 QX-200 Droplet Reader (Bio-rad; 186-4003). Results were quantified using the QuantaSoft

566 software (Bio-rad).

567

568 **Protrusion/cell body isolation**

569 Protrusion and cell bodies were isolated from serum-starved NIH/3T3 cells plated on

570 transwell inserts with 3.0 μm porous polycarabonate membrane (Corning) as previously

571 described[11]. Extracts were isolated using Trizol LS. Isolated RNAs were then quantified using the

nanoString nCounter analysis platform and a custom-made codeset, according to the manufacturer's instructions.

Western blot

For western blotting the following primary antibodies were used: rabbit anti-NET1(1:1000; Bethyl; A303-138A) and mouse anti-α-tubulin (1:2000; Sigma; T6199). Anti-rabbit and anti-mouse secondary antibodies from Li-Cor were used at 1:10,000. Membranes were scanned using an Odyssey fluorescent scanner (Li-Cor) and bands were quantified using ImageStudioLite (Li-Cor).

Human and primate tissues

De-identified human samples were collected from normal tissue following Mohs surgery for skin cancer removal. Frozen skin samples were collected and frozen in OCT before sectioning and confirmed to be normal by H&E staining. Under National Institutes of Health protocols, the use of biospecimens from de-identified discarded human tissue does not meet the regulatory criteria for human subject research and therefore institutional review board review or informed consent are waived.

Non-human primate tissues were obtained from the National Institute on Aging's (NIA) Nonhuman Primate Tissue Bank. Fresh frozen tongue biopsies were obtained from 14–24 year-old female and male *Papio Anubis* (Olive Baboons) in the process of necropsy.

Statistical analysis

Where relevant, data are shown as mean ± standard error of the mean (SEM). Individual measurements are shown with differing colors corresponding to individual experiments or animals. For statistical comparisons parametric tests were used to evaluate significant differences in normal distributed, homoscedastic datasets. Where either of these assumptions were not true, we instead performed non-parametric tests suitable for the data distribution. Specific statistical tests for each experiment are described in the figure captions.

References

1   Moor, A. E. *et al.* Global mRNA polarization regulates translation efficiency in the intestinal epithelium. *Science* **357**, 1299-1303 (2017). https://doi.org/10.1126/science.aan2399

2   Goering, R., Arora, A., Pockalny, M. C. & Taliaferro, J. M. RNA localization mechanisms transcend cell morphology. *Elife* **12** (2023). https://doi.org/10.7554/eLife.80040

3   Das, S., Vera, M., Gandin, V., Singer, R. H. & Tutucci, E. Intracellular mRNA transport and localized translation. *Nat Rev Mol Cell Biol* **22**, 483-504 (2021). https://doi.org/10.1038/s41580-021-00356-8

4   Bourke, A. M., Schwarz, A. & Schuman, E. M. De-centralizing the Central Dogma: mRNA translation in space and time. *Mol Cell* **83**, 452-468 (2023). https://doi.org/10.1016/j.molcel.2022.12.030

5   Fazal, F. M. *et al.* Atlas of Subcellular RNA Localization Revealed by APEX-Seq. *Cell* **178**, 473-490 e426 (2019). https://doi.org/10.1016/j.cell.2019.05.027

6   Chouaib, R. *et al.* A Dual Protein-mRNA Localization Screen Reveals Compartmentalized Translation and Widespread Co-translational RNA Targeting. *Dev Cell* **54**, 773-791 e775 (2020). https://doi.org/10.1016/j.devcel.2020.07.010

7   Gasparski, A. N., Mason, D. E., Moissoglu, K. & Mili, S. Regulation and outcomes of localized RNA translation. *Wiley Interdiscip Rev RNA* **13**, e1721 (2022). https://doi.org/10.1002/wrna.1721

8   Miller, S. *et al.* Disruption of dendritic translation of CaMKIIalpha impairs stabilization of synaptic plasticity and memory consolidation. *Neuron* **36**, 507-519 (2002). https://doi.org/10.1016/s0896-6273(02)00978-9

9   Preitner, N. *et al.* APC is an RNA-binding protein, and its interactome provides a link to neural development and microtubule assembly. *Cell* **158**, 368-382 (2014). https://doi.org/10.1016/j.cell.2014.05.042

10   Mili, S., Moissoglu, K. & Macara, I. G. Genome-wide screen reveals APC-associated RNAs enriched in cell protrusions. *Nature* **453**, 115-119 (2008). https://doi.org/10.1038/nature06888

11   Wang, T., Hamilla, S., Cam, M., Aranda-Espinoza, H. & Mili, S. Extracellular matrix stiffness and cell contractility control RNA localization to promote cell migration. *Nat Commun* **8**, 896 (2017). https://doi.org/10.1038/s41467-017-00884-y

12   Pichon, X. *et al.* The kinesin KIF1C transports APC-dependent mRNAs to cell protrusions. *RNA* **27**, 1528-1544 (2021). https://doi.org/10.1261/rna.078576.120

13   Moissoglu, K. *et al.* RNA localization and co-translational interactions control RAB13 GTPase function and cell migration. *The EMBO journal* **39**, e104958 (2020). https://doi.org/10.15252/embj.2020104958

14   Chrisafis, G. *et al.* Collective cancer cell invasion requires RNA accumulation at the invasive front. *Proceedings of the National Academy of Sciences of the United States of America* **117**, 27423-27434 (2020). https://doi.org/10.1073/pnas.2010872117

15   Gasparski, A. N. *et al.* mRNA location and translation rate determine protein targeting to dual destinations. *Mol Cell* **83**, 2726-2738 e2729 (2023). https://doi.org/10.1016/j.molcel.2023.06.036

16   Moriarty, R. A., Mili, S. & Stroka, K. M. RNA localization in confined cells depends on cellular mechanical activity and contributes to confined migration. *iScience* **25**, 103845 (2022). https://doi.org/10.1016/j.isci.2022.103845

17   Norris, M. L. & Mendell, J. T. Localization of Kif1c mRNA to cell protrusions dictates binding partner specificity of the encoded protein. *Genes Dev* **37**, 191-203 (2023). https://doi.org/10.1101/gad.350320.122

18   Carr, H. S., Morris, C. A., Menon, S., Song, E. H. & Frost, J. A. Rac1 controls the subcellular localization of the Rho guanine nucleotide exchange factor Net1A to regulate focal adhesion formation and cell spreading. *Mol Cell Biol* **33**, 622-634 (2013). https://doi.org/10.1128/MCB.00980-12

19   Carr, H. S., Zuo, Y., Oh, W. & Frost, J. A. Regulation of focal adhesion kinase activation, breast cancer cell motility, and amoeboid invasion by the RhoA guanine nucleotide exchange factor Net1. *Mol Cell Biol* **33**, 2773-2786 (2013). https://doi.org/10.1128/MCB.00175-13

20   Dermit, M. *et al.* Subcellular mRNA Localization Regulates Ribosome Biogenesis in Migrating Cells. *Dev Cell* **55**, 298-313 e210 (2020). https://doi.org/10.1016/j.devcel.2020.10.006

21   Rezza, A. *et al.* Signaling Networks among Stem Cell Precursors, Transit-Amplifying Progenitors, and their Niche in Developing Hair Follicles. *Cell Rep* **14**, 3001-3018 (2016). https://doi.org/10.1016/j.celrep.2016.02.078

22   Joost, S. *et al.* The Molecular Anatomy of Mouse Skin during Hair Growth and Rest. *Cell Stem Cell* **26**, 441-457 e447 (2020). https://doi.org/10.1016/j.stem.2020.01.012

23   Laurin, M. *et al.* An RNAi screen unravels the complexities of Rho GTPase networks in skin morphogenesis. *Elife* **8** (2019). https://doi.org/10.7554/eLife.50226

24   Geary, W. A. & Cooper, P. H. Proliferating cell nuclear antigen (PCNA) in common epidermal lesions. An immunohistochemical study of proliferating cell populations. *J Cutan Pathol* **19**, 458-468 (1992). https://doi.org/10.1111/j.1600-0560.1992.tb01598.x

25   Squier, C. A. & Kremer, M. J. Biology of oral mucosa and esophagus. *J Natl Cancer Inst Monogr*, 7-15 (2001). https://doi.org/10.1093/oxfordjournals.jncimonographs.a003443

26   Burgeson, R. E. & Christiano, A. M. The dermal-epidermal junction. *Curr Opin Cell Biol* **9**, 651-658 (1997). https://doi.org/10.1016/s0955-0674(97)80118-4

27   Roig-Rosello, E. & Rousselle, P. The Human Epidermal Basement Membrane: A Shaped and Cell Instructive Platform That Aging Slowly Alters. *Biomolecules* **10** (2020). https://doi.org/10.3390/biom10121607

28   Rousselle, P., Laigle, C. & Rousselet, G. The basement membrane in epidermal polarity, stemness, and regeneration. *Am J Physiol Cell Physiol* **323**, C1807-C1822 (2022). https://doi.org/10.1152/ajpcell.00069.2022

29   Adamo, C. S., Zuk, A. V. & Sengle, G. The fibrillin microfibril/elastic fibre network: A critical extracellular supramolecular scaffold to balance skin homoeostasis. *Exp Dermatol* **30**, 25-37 (2021). https://doi.org/10.1111/exd.14191

30   Selby, C. C. An electron microscope study of the epidermis of mammalian skin in thin sections. I. Dermo-epidermal junction and basal cell layer. *J Biophys Biochem Cytol* **1**, 429-444 (1955). https://doi.org/10.1083/jcb.1.5.429

31   Lavker, R. M. & Sun, T. T. Heterogeneity in epidermal basal keratinocytes: morphological and functional correlations. *Science* **215**, 1239-1241 (1982). https://doi.org/10.1126/science.7058342

692   32   Roig-Rosello, E. *et al.* Dermal stiffness governs the topography of the epidermis and the underlying basement membrane in young and old human skin. *Aging Cell* **23**, e14096 (2024). https://doi.org/10.1111/acel.14096

695   33   Schmelzer, C. E. H. & Duca, L. Elastic fibers: formation, function, and fate during aging and disease. *FEBS J* **289**, 3704-3730 (2022). https://doi.org/10.1111/febs.15899

697   34   Haller, S. J. & Dudley, A. T. Extracellular mechanotransduction. *J Gen Physiol* **154** (2022). https://doi.org/10.1085/jgp.202113026

699   35   Wang, M. C., Lu, Y. & Baldock, C. Fibrillin microfibrils: a key role for the interbead region in elasticity. *J Mol Biol* **388**, 168-179 (2009). https://doi.org/10.1016/j.jmb.2009.02.062

702   36   Kelley, M. *et al.* FBN-1, a fibrillin-related protein, is required for resistance of the epidermis to mechanical deformation during C. elegans embryogenesis. *Elife* **4** (2015). https://doi.org/10.7554/eLife.06565

705   37   Loeys, B. L. *et al.* Mutations in fibrillin-1 cause congenital scleroderma: stiff skin syndrome. *Sci Transl Med* **2**, 23ra20 (2010). https://doi.org/10.1126/scitranslmed.3000488

708   38   Moissoglu, K. *et al.* A KIF1C-CNBP motor-adaptor complex for trafficking mRNAs to cell protrusions. *bioRxiv* (2024). https://doi.org/10.1101/2024.06.26.600878

710   39   Miroshnikova, Y. A. *et al.* Adhesion forces and cortical tension couple cell proliferation and differentiation to drive epidermal stratification. *Nat Cell Biol* **20**, 69-80 (2018). https://doi.org/10.1038/s41556-017-0005-z

713   40   Aragona, M. *et al.* Mechanisms of stretch-mediated skin expansion at single-cell resolution. *Nature* **584**, 268-273 (2020). https://doi.org/10.1038/s41586-020-2555-7

715   41   Charbonneau, N. L. *et al.* Microfibril structure masks fibrillin-2 in postnatal tissues. *J Biol Chem* **285**, 20242-20251 (2010). https://doi.org/10.1074/jbc.M109.087031

717   42   Watson, R. E., Griffiths, C. E., Craven, N. M., Shuttleworth, C. A. & Kielty, C. M. Fibrillin-rich microfibrils are reduced in photoaged skin. Distribution at the dermal-epidermal junction. *J Invest Dermatol* **112**, 782-787 (1999). https://doi.org/10.1046/j.1523-1747.1999.00562.x

721   43   Schmidt, A. & Hall, A. The Rho exchange factor Net1 is regulated by nuclear sequestration. *J Biol Chem* **277**, 14581-14588 (2002). https://doi.org/10.1074/jbc.M111108200

724   44   Song, E. H. *et al.* Acetylation of the RhoA GEF Net1A controls its subcellular localization and activity. *J Cell Sci* **128**, 913-922 (2015). https://doi.org/10.1242/jcs.158121

727   45   Nakaya, Y., Sukowati, E. W., Wu, Y. & Sheng, G. RhoA and microtubule dynamics control cell-basement membrane interaction in EMT during gastrulation. *Nat Cell Biol* **10**, 765-775 (2008). https://doi.org/10.1038/ncb1739

730   46   Wang, S. *et al.* NET1 is a critical regulator of spindle assembly and actin dynamics in mouse oocytes. *Reprod Biol Endocrinol* **22**, 5 (2024). https://doi.org/10.1186/s12958-023-01177-4

733   47   Amano, M. *et al.* Phosphorylation and activation of myosin by Rho-associated kinase (Rho-kinase). *J Biol Chem* **271**, 20246-20249 (1996). https://doi.org/10.1074/jbc.271.34.20246

736 48   Hinnant, T., Ning, W. & Lechler, T. Compartment specific responses to contractility in the
737   small intestinal epithelium. *PLoS Genet* **20**, e1010899 (2024).
738   https://doi.org/10.1371/journal.pgen.1010899
739 49   Ning, W., Muroyama, A., Li, H. & Lechler, T. Differentiated Daughter Cells Regulate
740   Stem Cell Proliferation and Fate through Intra-tissue Tension. *Cell Stem Cell* **28**, 436-452
741   e435 (2021). https://doi.org/10.1016/j.stem.2020.11.002
742 50   Ambros, V. MicroRNAs and developmental timing. *Curr Opin Genet Dev* **21**, 511-517
743   (2011). https://doi.org/10.1016/j.gde.2011.04.003
744 51   Khoo, B. & Krainer, A. R. Splicing therapeutics in SMN2 and APOB. *Curr Opin Mol*
745   *Ther* **11**, 108-115 (2009).
746 52   Zuo, Y., Berdeaux, R. & Frost, J. A. The RhoGEF Net1 is required for normal mammary
747   gland development. *Mol Endocrinol* **28**, 1948-1960 (2014).
748   https://doi.org/10.1210/me.2014-1128
749 53   Lee, B. *et al.* Linkage of Marfan syndrome and a phenotypically related disorder to two
750   different fibrillin genes. *Nature* **352**, 330-334 (1991). https://doi.org/10.1038/352330a0
751 54   Schindelin, J. *et al.* Fiji: an open-source platform for biological-image analysis. *Nat*
752   *Methods* **9**, 676-682 (2012). https://doi.org/10.1038/nmeth.2019
753 55   Magsipoc, E., Zhao, Q. & Grasselli, G. 2D and 3D Roughness Characterization. *Rock*
754   *Mechanics and Rock Engineering* **53**, 1495-1519 (2020). https://doi.org/10.1007/s00603-
755   019-01977-4
756 56   Stueland, M., Wang, T., Park, H. Y. & Mili, S. RDI Calculator: An Analysis Tool to
757   Assess RNA Distributions in Cells. *Sci Rep* **9**, 8267 (2019).
758   https://doi.org/10.1038/s41598-019-44783-2
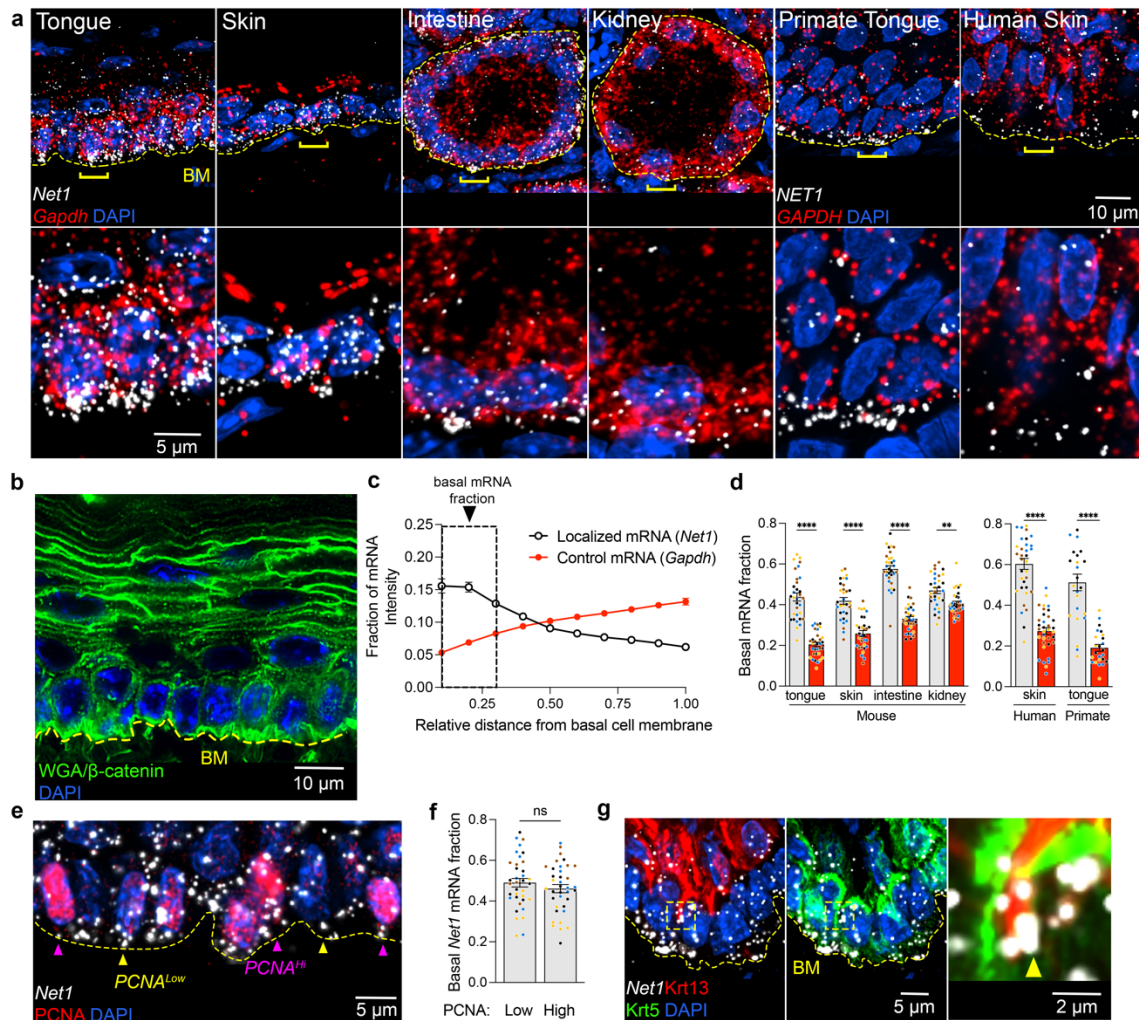
Fig. 1: Conserved basal localization of *Net1* mRNA across epithelial architectures and cellular contexts. a, Upper panels: Representative images of *Net1* and *Gapdh* mRNAs in mouse tongue, skin, intestine, and kidney as well as images of primate tongue and human skin. Dashed yellow line indicates the basement membrane (BM). Bottom panels: zoomed in regions around areas indicated by brackets. **b**, Representative image of wheat germ agglutin (WGA) and β-catenin, as well as nuclei by DAPI in mouse tongue. Staining was used for segmentation of tissue layer boundaries. **c**, *Net1* and *Gapdh* fluorescent intensity in subsections starting at the BM to the most apical portion of the cell layer. Boxed region indicates RNA amount defined as the basal mRNA fraction. **d**, *Net1 mRNA* (white bars) exhibits basal enrichment relative to *Gapdh* (red bars) across tissues and species. **e**, Visualization of *Net1* localization and PCNA in mouse tongue. Yellow arrowheads indicate PCNA^{Low} and pink arrowheads indicate PCNA^{Hi} cells. **f**, Basal fraction of *Net1* in PCNA^{Hi} vs PCNA^{Lo} cells. **g**, Representative images of basal (Krt5+) and spinous (Krt13+) cells with an inset showing *Net1* mRNA localized to the basal tips of Krt13+ cells (yellow arrowhead). Bar graph data are measurements from individual tissue regions (ROIs) with mean ± SEM; n = 31 (d) or 36 (f) ROIs from N = 3-4 mice. Data from individual mice are represented with different colors. ** P ≤ 0.01, **** P ≤ 0.0001, ns: non-significant by Brown-Forsythe and Welch ANOVA followed by Dunnett's T3 multiple comparison test (d), or unpaired two-tailed Student's *t*-test (f).
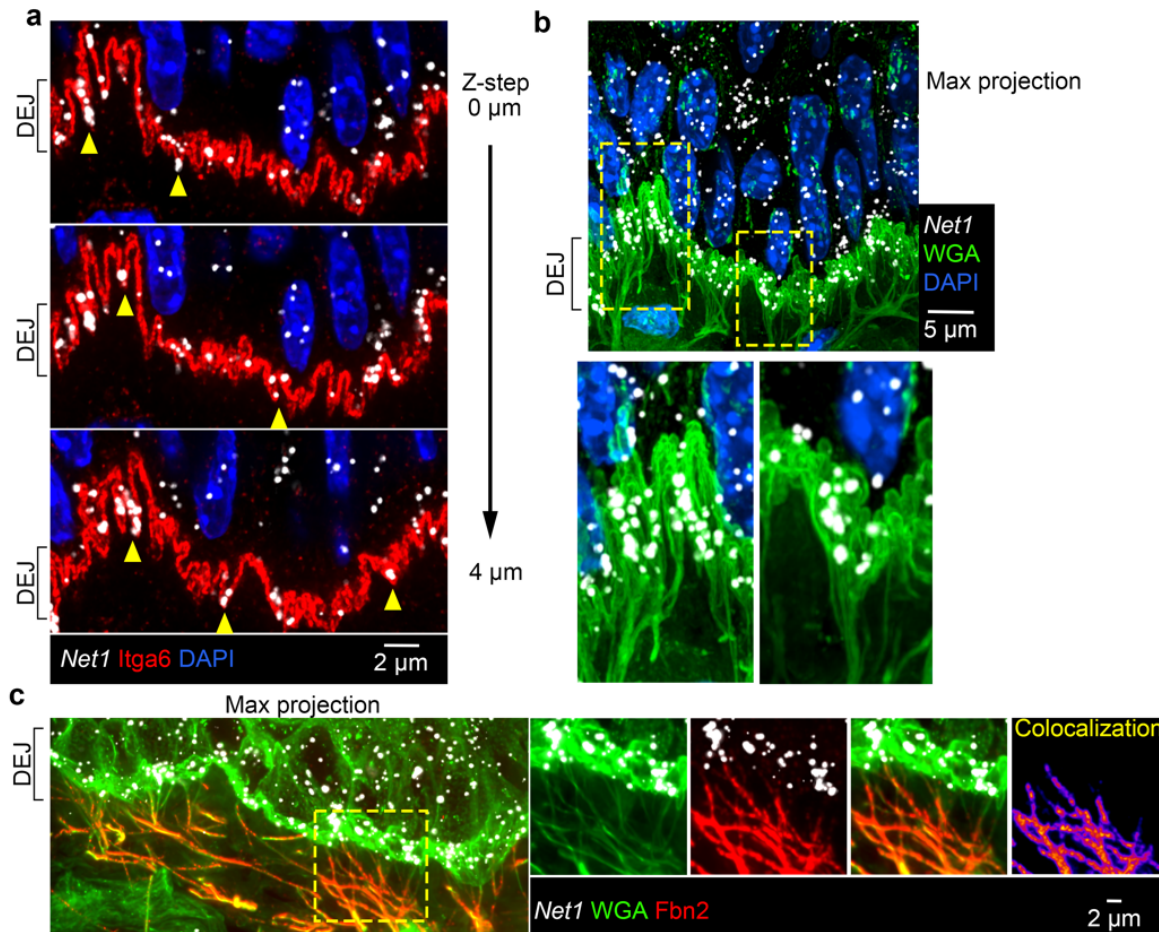
Fig. 2: *Net1* **accumulates in keratinocyte protrusion-like structures connected to microfibrils at the DEJ**. **a**, Representative images of mouse tongue showing *Net1* at the DEJ. The basal keratinocyte cell membrane is visualized by Itga6 in sequential optical Z-slices. Arrowheads indicate *Net1* mRNA at protrusion-like structures. **b**, *Net1* and WGA staining of mouse tongue. Bottom panels: zoomed in regions, indicated by yellow boxes, highlighting fibers connecting with the basal keratinocyte cell membrane. Image is a max-intensity projection of ~3 um in the z-axis. **c**, Mouse tongue section stained for *Net1* mRNA, WGA and Fbn2. Right panels show individual channels and overlay from boxed region. Colocalization panel shows pixel intensity overlap between WGA and Fbn2 channels.
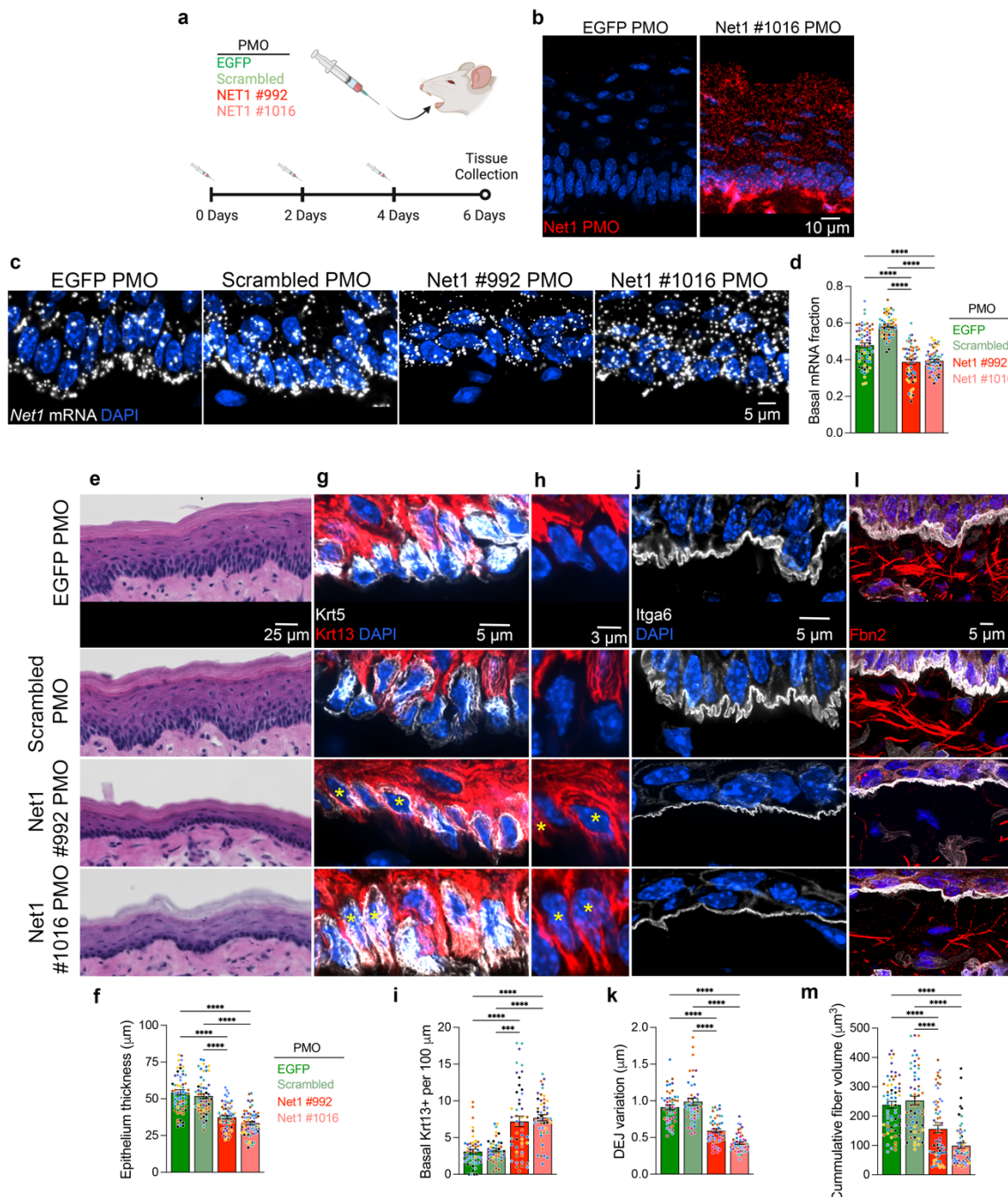
Fig. 3: *Net1* **mRNA localization controls epithelial homeostasis and keratinocyte interaction with the DEJ. a**, Schematic of PMO injection protocol into the ventral side of mouse tongues using sequences targeting *EGFP* or the *Net1* 3'UTR at positions #992 and #1016, as well as a scrambled version of #992. **b**, PMO uptake into the tongue epithelium was visualized using Net1 #1016 PMO-specific probes. **c**, Visualization of *Net1* distribution in PMO injected tongues. **d**, Basal *Net1* mRNA fraction in PMO treated tissues. **e**, Visualization of overall oral epithelium

architecture using H&E on ventral portion of the tongue. **f**, Measurement of tongue epithelial thickness. **g**, Visualization of basal (Krt5) and spinous (Krt13) keratinocytes in the basal compartment of tongue epithelium. **h**, Select areas from (g). Krt13 channel is only shown to highlight examples of Krt5+/Krt13- basal cells in control PMO treated tongues and Krt5+/Krt13+ in Net1 PMO treated tongues. Asterisks indicate double positive cells. **i**, Number of Krt5+/Krt13+ cells in the basal compartment normalized to DEJ length. **j**, Visualization of DEJ using Itga6 in PMO treated mouse tongues. **k**, Measurement of DEJ topographical variation. **l**, Visualization of Fbn2+ fibers in PMO-treated tongues. **m**, Quantification of DEJ proximal Fbn2+ fiber volume. Bar graph data are measurements from individual tissue regions (ROIs) with mean ± SEM; n = 42-64 ROIs from N = 7-8 mice per condition. Data from individual mice are represented with different colors. *** $P \leq 0.001$ and **** $P \leq 0.0001$ by Brown-Forsythe and Welch ANOVA followed by Dunnett's T3 multiple comparison test (d) or Kruskal-Wallis ANOVA followed by Dunn's multiple comparison tests (f,i,k,m).
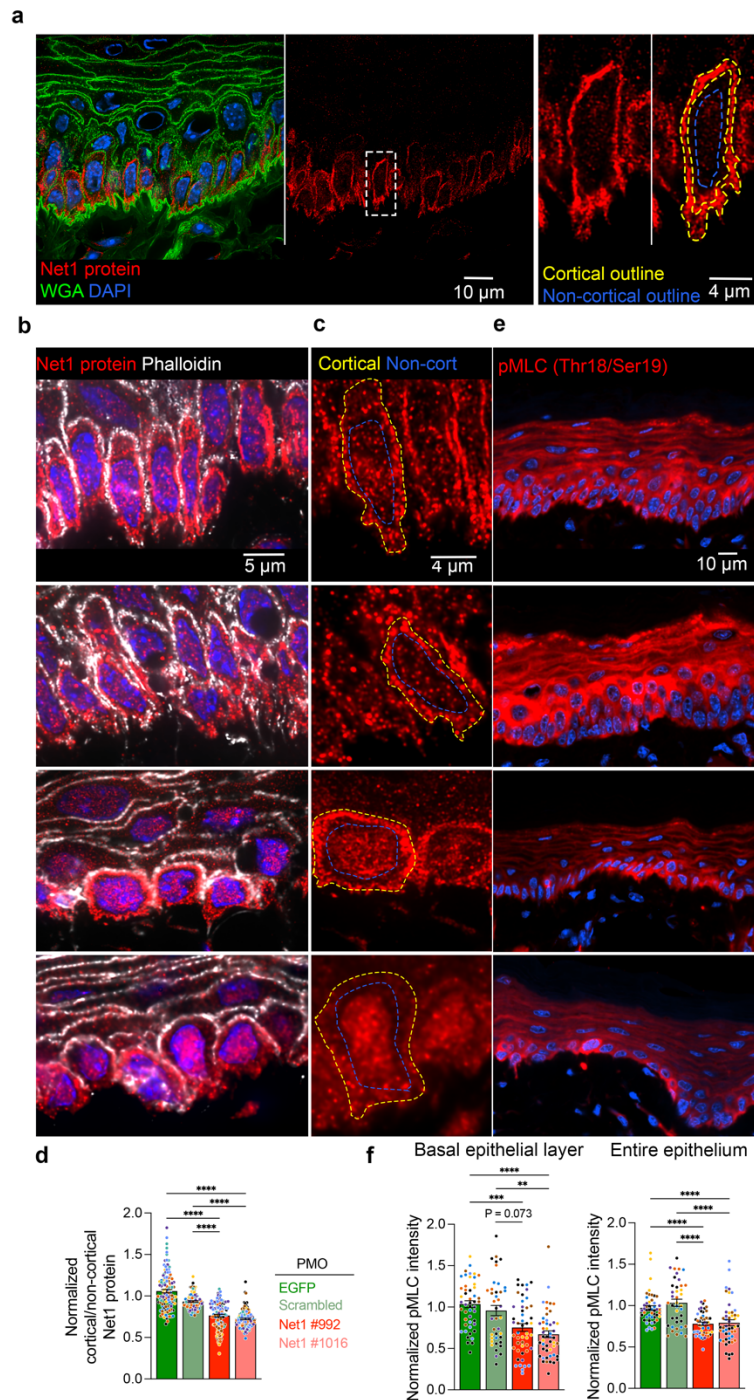
Fig. 4: _Net1_ mRNA localization regulates Net1 protein distribution and activity _in vivo_. a, Visualization of Net1 protein and WGA in mouse tongue keratinocytes. Left panel: overlay. Middle panel: Net1 channel showing predominant expression in basal keratinocytes. Right panels: zoom in of boxed region. Dashed yellow and blue lines indicate cortical and non-cortical regions, respectively, used for Net1 distribution measurements. **b**, Visualization of Net1 protein with

phalloidin as a marker of the cell cortex in PMO treated tissues. **c**, High magnification visualization of Net1 protein where the cell cortex and non-cortical region are indicated by yellow and blue broken lines, respectively. **d**, Quantification of Net1 protein distribution (ratio of cortical to non-cortical mean intensity). **e**, Visualization of MLC2 phosphorylation (pMLC) in the mouse epithelium. **f**, Quantification of mean pMLC2 fluorescent intensity for basal keratinocytes (left) and the entire oral epithelium (right). Bar graph data are individual measurements with mean $\pm$ SEM; n=105-120 cells (d) or 40-48 ROIs (f) from N = 7-8 mice per condition. Data from individual mice are represented with different colors. ** $P \leq 0.01$, *** $P \leq 0.001$, **** $P \leq 0.0001$ by Kruskal-Wallis ANOVA followed by Dunn's multiple comparison test.
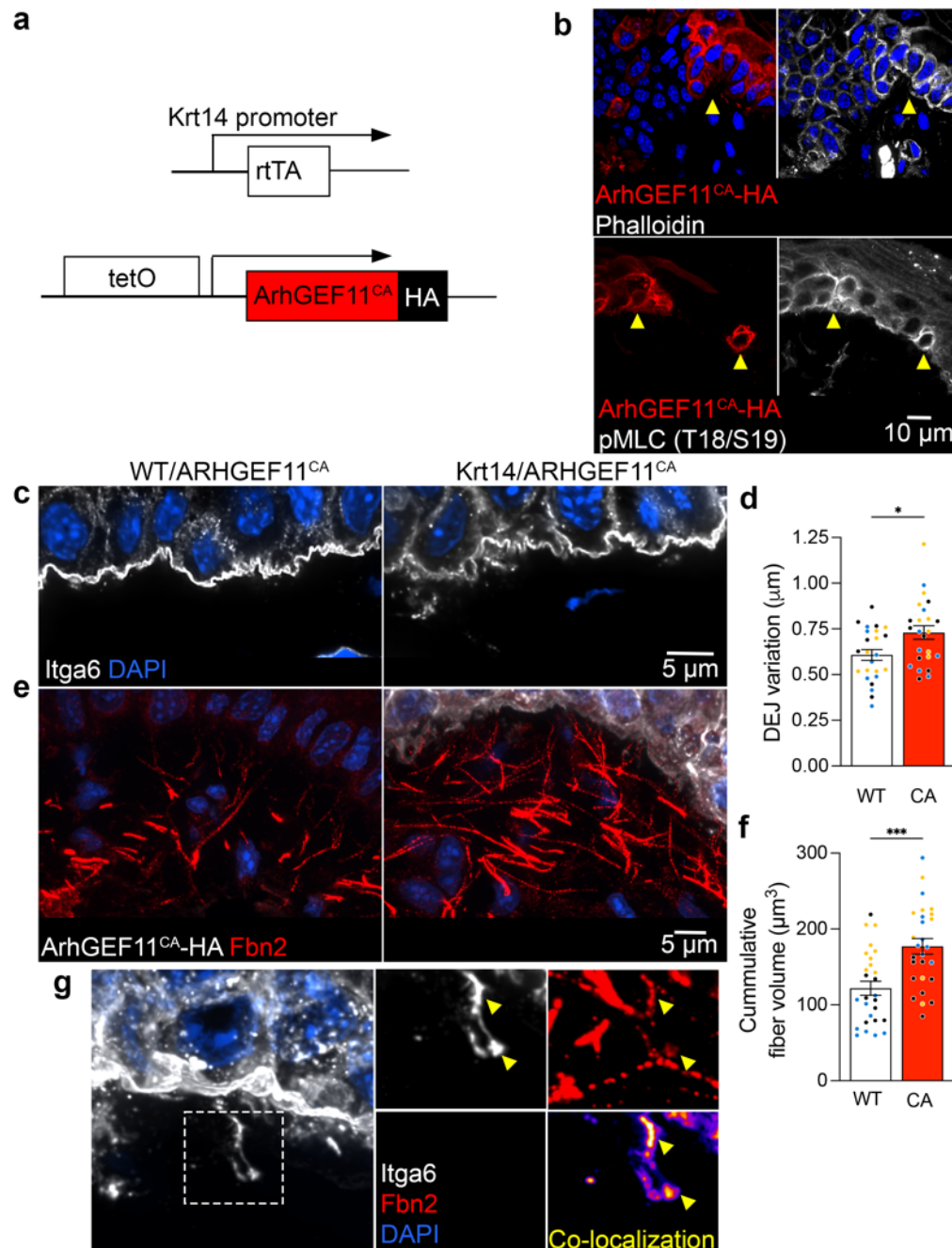
Fig. 5: RhoA activation in basal keratinocytes remodels the DEJ. a, Schematic of ArhGEF11^{CA}-HA expression under the control of tetracycline-inducible promoter where the reverse tetracycline-controlled transactivator is expressed in basal epithelial cells (Krt14-rtTA). **b**, Visualization of the actin cytoskeleton (phalloidin) and pMLC in ArhGEF11^{CA}-HA-expressing cells. Mosaic expression of ArhGEF11^{CA} is indicated by yellow arrowheads. **c**, Visualization of the DEJ by Itga6 in WT or ArhGEF11^{CA} mice. **d**, Quantification of DEJ variation in knock-in mice.

Measurements in ArhGEF11^{CA} (CA) mice were made in regions with continuous HA expression in basal keratinocytes across an analysis ROI. **e**, Visualization of HA and Fbn2 at the DEJ of WT or ArhGEF11^{CA} mice. **f**, Quantification of Fbn2 volume proximal to the DEJ. **g**, Left panel: example of an ArhGEF11^{CA}-expressing cell exhibiting extension of the plasma membrane below the DEJ after supraphysiologic induction of RhoA activation. Plasma membrane is stained through Itga6. Right panels: Boxed region showing also Fbn2 staining and co-localization between the two channels. Yellow arrowheads indicate areas of high Itga6-Fbn2 co-localization. Bar graph data are measurements from individual ROIs with mean ± SEM; n = 24 (d) or 27 (f) ROIs from N = 3 mice. Data from individual mice are represented with different colors. * P < 0.05, *** P < 0.001 by unpaired two-tailed Student's *t*-test.
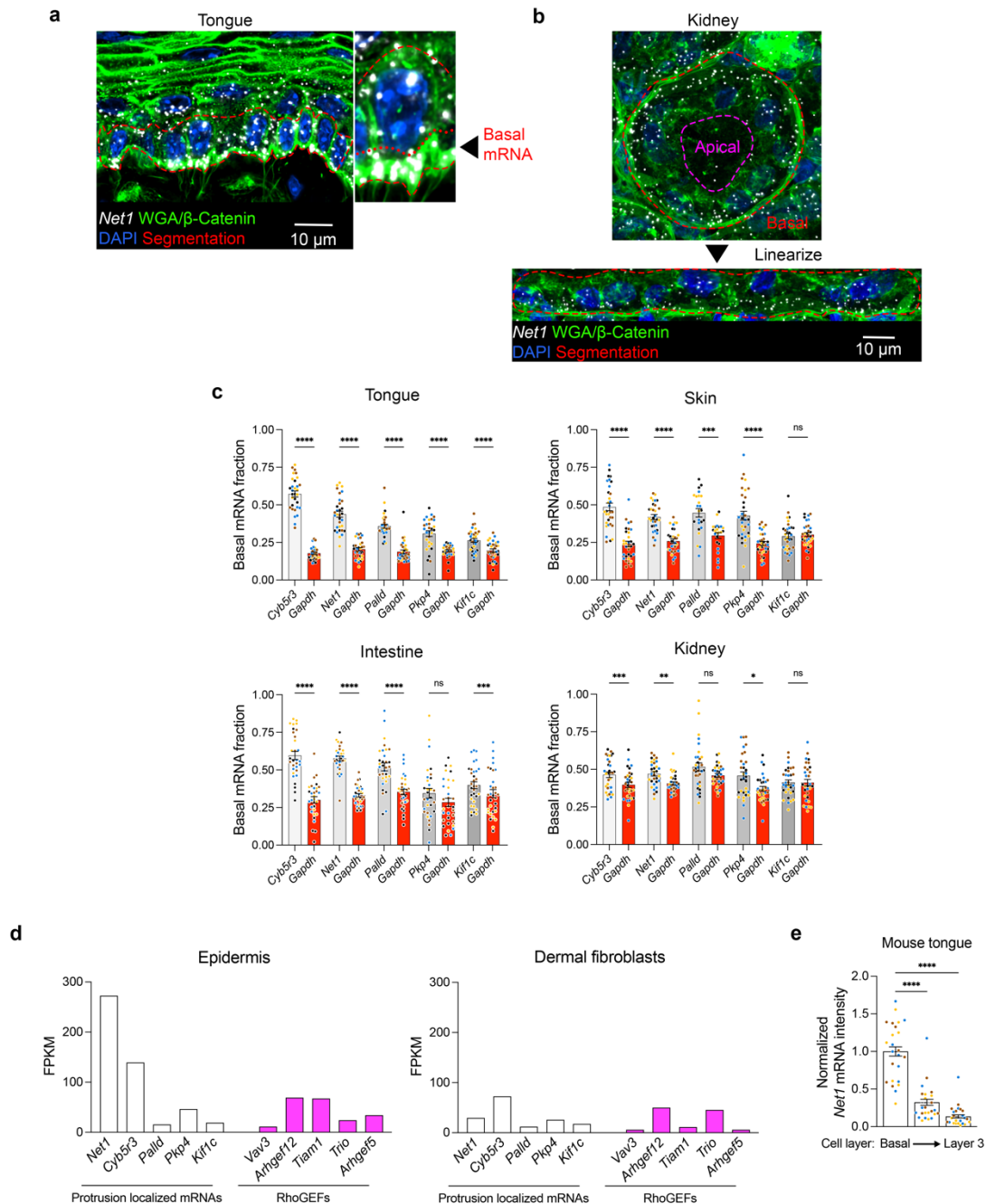
Extended Data Fig. 1: Protrusion localized mRNAs are basally localized across architecturally distinct tissues. a, Representative image of mouse tongue tissue stained for *Net1* mRNA and a combination of WGA and β-catenin. Manual segmentation of the basal cell layer is indicated by a red dashed line. The zoomed in inset highlights the position of the bottom 30% used to define the basal mRNA fraction. **b**, Representative tubular epithelial sheet from the kidney stained for *Net1* mRNA and a combination of WGA and β-catenin. For analysis, the image was

first linearized and subsequently analyzed using the approach taken in stratified tissues. **c**, Basal mRNA fraction of several protrusion-localized mRNAs (*Cyb5r3*, *Net1*, *Palld*, *Pkp4*, and *Kif1c*; grey bars) and of the *Gapdh* control mRNA (red bars) in mouse tongue, skin, intestine, and kidney. **d**, Relative fluorescent intensity of *Net1* mRNA in tongue keratinocytes from the 1st (basal), 2nd, and 3rd epithelail layers. **e**, Protrusion-localized and RhoGEF mRNA expression in the skin epidermis vs. dermal fibroblasts derived from published datasets. *Net1* expression is notably higher in the epidermis to the point where it qualifies as a signature gene for the basal keratinocytes of the skin. Bar graph data are measurements from individual ROIs with mean ± SEM; n = 27-32 ROIs from N = 3-4 mice. Data from individual mice are represented with different colors. * $P < 0.05$, ** $P < 0.01$, *** $P < 0.001$, **** $P < 0.0001$ by repeated measures ANOVA followed by Sidak's multiple comparisons test (c) or Kruskal-Wallis ANOVA followed by Dunn's multiple comparisons test (d).
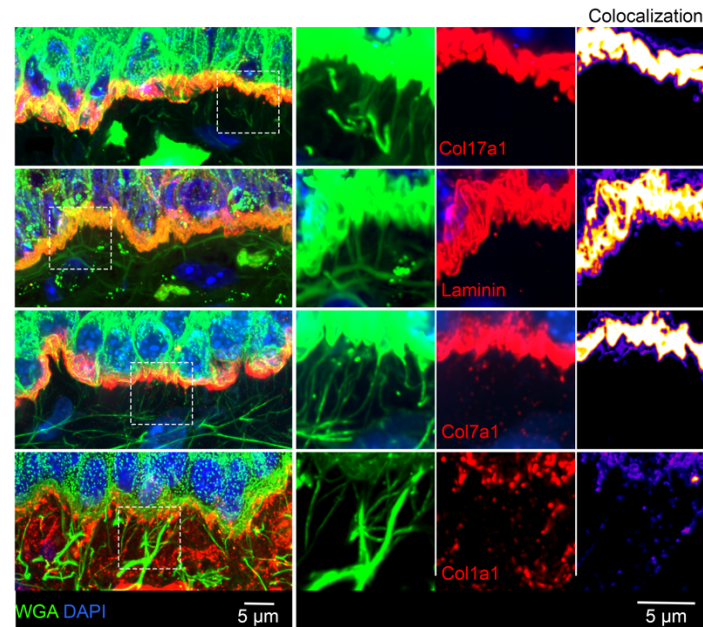
Extended Data Fig. 2: DEJ fibers are not comprised of hemidesmosome, basement membrane, or anchoring components. Representative images of mouse tongue tissue stained with WGA as well as with a panel of DEJ antibodies against Col17a1, pan-laminin, Col7a1, or Col1a1. Left panels: channel overlay images. Middle panels: individual channels (WGA:green; DEJ components: red) for the magnified boxed regions. Colocalization panels show pixel intensity overlap between WGA and DEJ channels. There was modest co-localization between DEJ fibers and Col1a1. Other DEJ components overlap with WGA at the region of the plasma membrane but not with WGA+ fibers below the DEJ.
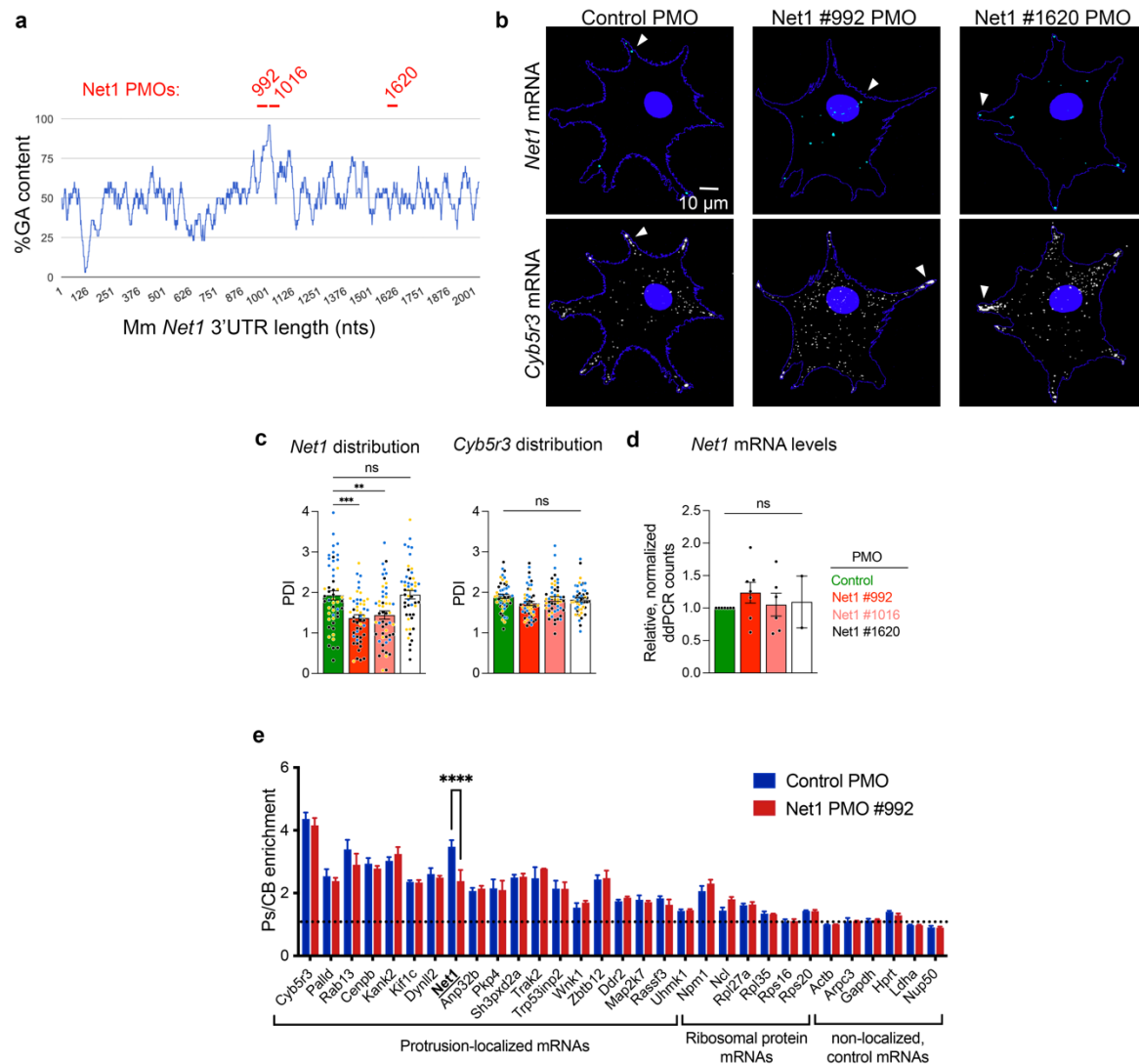
Extended Data Fig. 3: PMOs targeting the Mm *Net1* GA-rich region specifically alter *Net1* mRNA localization. a, GA content in 30nt windows along the *Net1* 3'UTR. Experimental Net1 PMOs were designed to target the *Net1* GA-rich region (#992 and #1016) or a different region (#1620) as a control (red lines indicate PMO locations). **b**, Representative images of *Net1* and *Cyb5r3* mRNA distribution in NIH/3T3 fibroblasts transfected with Control or Net1 targeting PMOs. Cell boundaries are indicated by a blue line. Arrowheads point to areas of RNA accumulation. Note that Net1 #992 PMO leads to perinuclear *Net1*. **c**, *Net1* and *Cyb5r3* mRNA distribution after PMO transfection as measured by a peripheral distribution index (PDI). PDI is an intensity weighted measure of the distribution of an RNA population relative to the center of the nucleus. A value above 1 is more peripheral, 1 is diffuse, and a value below 1 is a more perinuclear mRNA. n = 51 cells in 3 independent biological replicates. Data from independent

experiments are shown in different colors. **d**, ddPCR count of *Net1* mRNA normalized to a housekeeping gene. n=2-7 biological and technical replicates **e**, Protrusion (Ps) and cell body (CB) fractions were isolated from 3T3 cells extending protrusions through transwell pores. The indicated mRNAs were detected by nanostring analysis to calculate a Ps/CB enrichment ratio. n=3. Bar graph data are individual measurements with mean ± SEM. ** P < 0.01, *** P < 0.001, **** P < 0.0001, ns: non-significant by ordinary one-way ANOVA followed by Dunnett's multiple comparison test (c), mixed effects analysis with Dunnett's multiple comparison test (d), or 2-way ANOVA followed by Sidak's multiple comparison test (e).
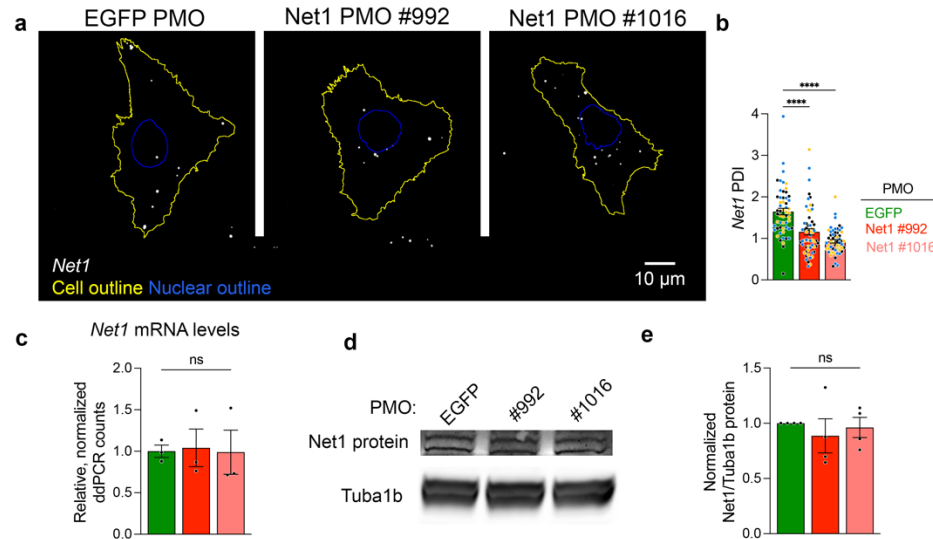
Extended Data Fig. 4: *Net1* **PMOs alter** *Net1* **mRNA localization without affecting mRNA or protein abundance in mouse keratinocytes** *in vitro*. **a**, Representative images of *Net1* mRNA localization in immortalized mouse keratinocytes treated with PMOs targeting *EGFP* or *Net1* mRNAs. **b**, Peripheral distribution of *Net1* measured by PDI in PMO treated cells. n = 56 cells in 3 independent biological replicates. Data from independent experiments are shown in different colors. **c**, ddPCR count of *Net1* mRNA normalized to a housekeeping gene *GusB*. n=3. **d**, Representative images of western blot detecting Net1 and Tuba1b protein from whole keratinocyte lysates. **e**, Quantification of Net1 protein normalized to Tuba1b. n=4. Bar graph data are individual measurements with mean ± SEM. **** $P < 0.0001$, ns: non-significant by Kruskal-Wallis ANOVA followed by Dunn's multiple comparison test (b), or ordinary one-way ANOVA followed by Dunnett's multiple comparison test (c,e).
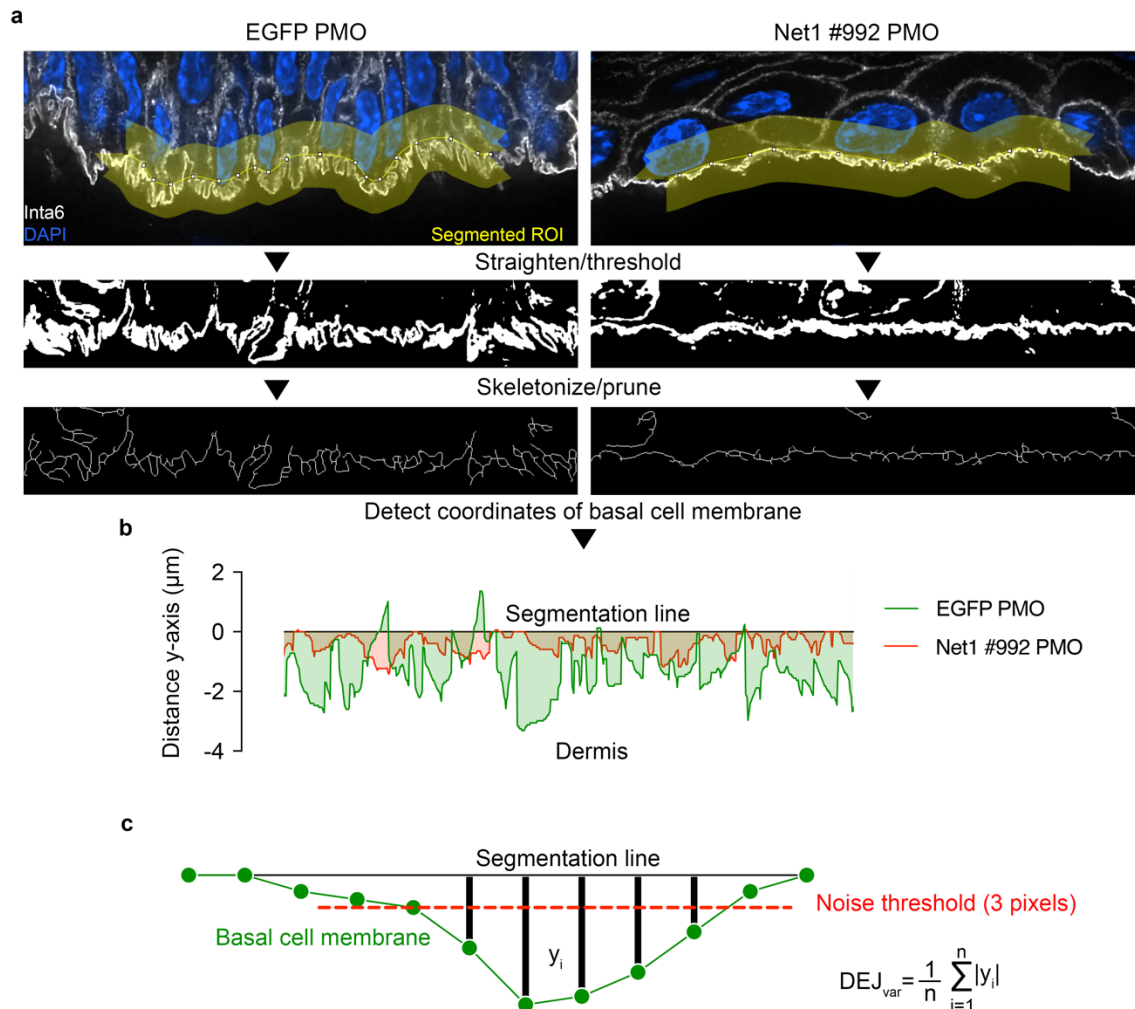
Extended Data Fig. 5: Analysis pipeline for measuring membrane topographical variation in the DEJ. a, For analysis, individual optical slices from tissue sections stained for Itga6 were used. Regions of the DEJ were isolated by drawing a segmented line ROI (120 pixel (7.8 μm) wide) centered on the basal cell membrane. The upper limits of protrusion-like structures were used as a reference. The ROI was digitally straightened and thresholded followed by skeletonization and pruning of incomplete membrane segments. **b**, From the mask in (**a**) the most basal coordinates in each x-position were derived. These basal coordinates were used to estimate y-axis variation relative to the original segmentation line. The graphical representation depicts x-position coordinates for the representative images from EGFP or Net1 PMO treated tissue. **c**, DEJ variation (DEJ$_{var}$) was calculated as the average distance between the basal cell membrane coordinates (described in **b**) and the segmentation line. To limit the degree to which segmentation variability can influence the result a noise threshold of 3 pixels (~.2 μm) was applied so that vertical

displacement less than 3 pixels were set to 0. Multiple optical slices and segmentation lines were used to get a variability estimate across at least 100 μm of the DEJ for a single ROI, at least 5 ROIs were measured per animal.
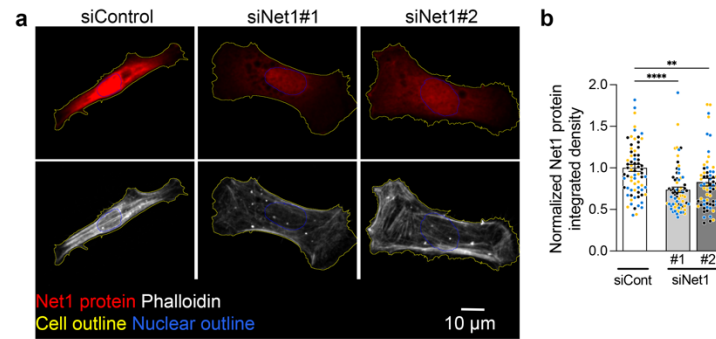
Extended Data Fig. 6: Net1 antibody validation for immunofluorescence in mouse keratinocytes. **a**, Representative Net1 protein immunofluorescence counterstained with phalloidin to visualize the actin cytoskeleton. Cells were treated with either a control or two different Net1 targeting siRNAs. Note: Net1 protein is predominantly nuclear in many *in vitro* cultured cells. **b**, Relative immunofluorescence intensity of Net1 protein. n = 22-28 cells per condition, N = 3 independent experiments. ** P < 0.01, **** P < 0.0001 by Kruskal-Wallis ANOVA followed by Dunn's multiple comparison test.
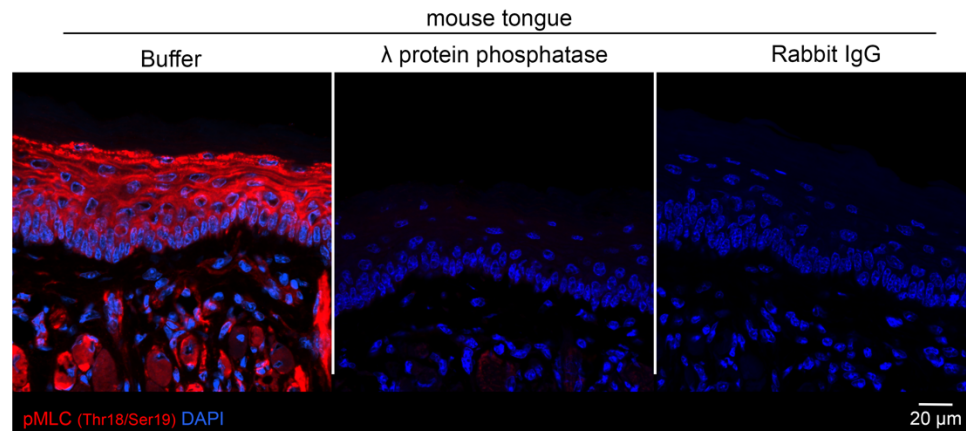
Extended Data Fig. 7: Myosin light chain (Thr18/Ser19) phosphorylation can be detected *in vivo* by immunofluorescence. Fixed mouse tongue sections were treated with λ protein phosphatase or buffer then stained with pMLC (Thr18/Ser19) primary antibody or Rabbit IgG. Immunofluorescent detection using an anti-rabbit secondary antibody indicated that pMLC primary antibody binding is diminished in tissues pre-treated with a serine, threonine, and tyrosine phosphatase.

Supplementary Video 1: *Net1* **mRNA and DEJ component staining in mouse tongue**. Representative serial optical sections of mouse tongue tissue. Upper panels: The basal cell membrane is visualized with the basal cell membrane marker Itga6, with or without overlay with *Net1* mRNA signal. Bottom panels: Visualization of the basal cell membrane and dermal fibers through WGA staining, with or without overlay with *Net1* mRNA signal. ~3 μm thick serial optical sections were acquired with a ~.065 μm step size.

Supplementary Video 2: *Net1* **mRNA and DEJ component staining in mouse tongue**. An additional representative serial optical sectioning of mouse tongue tissue. Upper panels: The basal cell membrane is visualized with the basal cell membrane marker Itga6, with or without overlay with *Net1* mRNA signal. Bottom panels: Visualization of the basal cell membrane and dermal fibers through WGA staining, with or without overlay with *Net1* mRNA signal. ~3 μm thick serial optical sections were acquired with a ~.065 μm step size.

Extended Data Table 1: PMO and siRNA sequences used *in vitro* and *in vivo*
Extended Data Table 2: Antibodies used for immunofluorescence
Extended Data Table 3: Probes for visualizing RNA